Analysis of Shear Layers in a Fluid with Temperature-Dependent Viscosity

Donald J. Estep,*,[1] Sjoerd M. Verduyn Lunel,†,[2] and Roy D. Williams‡

*Department of Mathematics, Colorado State University, Fort Collins, Colorado 80523;
†Mathematisch Instituut, Universiteit Leiden, P.O. Box 9512, 2300 RA Leiden,
The Netherlands; and ‡Center for Advanced Computing Research, California
Institute of Technology, Pasadena, California 91125
E-mail: *estep@math.colostate.edu, †verduyn@math.leidenuniv.nl, ‡roy@willow.caltech.edu

The presence of viscosity normally has a stabilizing effect on the flow of a fluid. However, experiments show that the flow of a fluid in which viscosity decreases as temperature increases tends to form shear layers, narrow regions in which the velocity of the fluid changes sharply. In general, adiabatic shear layers are observed not only in fluids but also in thermo-plastic materials subject to shear at a high-strain rate and in combustion and there is widespread interest in modeling their formation. In this paper, we investigate a well-known model representing a basic system of conservation laws for a one-dimensional flow with temperature-dependent viscosity using a combination of analytical and numerical tools. We present results to substantiate the claim that the formation of shear layers can only occur in solutions of the model when the viscosity decreases sufficiently quickly as temperature increases and we further analyze the structure and stability properties of the layers. © 2001 Academic Press

Key Words: a posteriori error estimates; adaptive error control; blow-up, conservation laws; finite element methods; fluid flow; invariant rectangles; plane Couette flow; reaction–diffusion equations; residual errors; shear layers; temperature-dependent viscosity; thermal diffusion.

CONTENTS

1. INTRODUCTION

The broad goal of this paper is to explore the role of dissipation in the large-time behavior of systems of nonlinear hyperbolic conservation laws. In general, the nonlinear character of the conservation laws induces a destabilizing mechanism, while the presence of viscosity and thermal diffusion has the opposite effect. We examine this delicate competition in the context of one-dimensional fluid flow within the framework of thermomechanics.

It is generally conjectured that heat dissipation alone cannot prevent the formation of shocks; see Dafermos and Hsiao [11]. An important question is whether or not the combined dissipative effect of viscosity and thermal diffusion can counterbalance the destabilizing influence of nonlinearity and induce the existence of globally smooth solutions; see Dafermos and Hsiao [9] and Tzarvaras [25]. Most of the existing analysis in the literature is restricted to the case where the viscosity does not vary with temperature. It is possible to perform some rigorous analysis in this case, but physically this is a rather crude assumption.

To elucidate the effects of the dependence of the viscosity on temperature and in particular to determine if the dependence of viscosity upon temperature can destabilize the flow of a fluid, Dafermos and Hsiao ([10]) proposed a test problem that models an adiabatic rectilinear shearing flow in an incompressible Newtonian viscous fluid between parallel plates with one plate moving at a constant distance from the other plate; see Fig. 1. We choose Cartesian coordinates so that the x-axis is perpendicular to the plates located at $x = 0$ and $x = 1$. We assume that the plate at $x = 0$ is at rest and the plate at $x = 1$ moves with constant velocity V in a direction orthogonal to x and that between the plates, the flow is parallel to the plates and uniform in the directions orthogonal to x. The Lagrangian description of the balance laws of mass, momentum, and energy with reference density $\rho_0 = 1$ yields

$$u_t(x, t) - v_x(x, t) = 0, \quad 0 < x < 1, \ 0 < t,$$
$$v_t(x, t) - \sigma_x(x, t) = 0, \quad 0 < x < 1, \ 0 < t, \quad (1)$$
$$(e(x, t) + \frac{1}{2}v(x, t)^2)_t - (\sigma(x, t)v(x, t))_x + q_x(x, t) = 0, \quad 0 < x < 1, \ 0 < t,$$

where u denotes the deformation gradient, v the velocity, σ the shear stress, e the internal energy, and q the heat flux. Under the assumption of an adiabatic shearing flow in an incompressible Newtonian viscous fluid and normalizing so that the density and the specific heat are one, the conservation laws from (1) reduce to

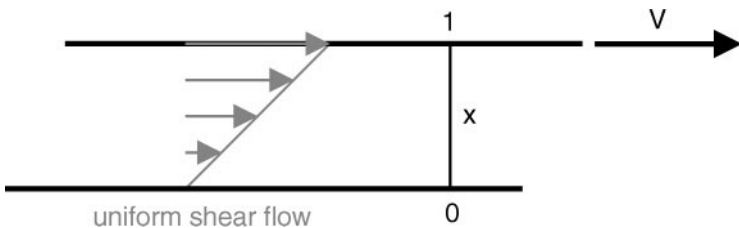$$v_t = \sigma_x \quad \text{and} \quad e_t = \sigma v_x. \quad (2)$$

FIG. 1. The one-dimensional model of shear flow.

Internal energy and viscosity are determined by temperature θ via known constitutive relations, $e = \hat{e}(\theta)$ and $\mu = \hat{\mu}(\theta)$. In typical fluids, $\hat{e}(\theta)$ is increasing and convex; the function $\hat{\mu}(\theta)$ is typically increasing in gases and decreasing in liquids. It is convenient to eliminate θ between $e = \hat{e}(\theta)$ and $\mu = \hat{\mu}(\theta)$ and consider viscosity as a known function of the internal energy. With this in mind, for simplicity we write θ for the internal energy and refer to it as the temperature.

For a constitutive relation, we assume that the fluid is linearly viscous; that is, the shear stress is related to the temperature and velocity gradient as follows

$$\sigma = \mu(\theta)v_x. \tag{3}$$

The same model has been proposed by Tzavaras ([23]) to study the destabilizing effect of thermal softening in solids during plastic shearing. For non-Newtonian fluids the constitutive relation reads

$$\sigma = \mu(\theta)|v_x|v_x^{n-1}, \quad n \geq 1. \tag{4}$$

This constitutive law is appropriate for a solid in a plastic region exhibiting thermal softening and strain rate sensitivity (measured by the parameter n) but no strain hardening. More general models that include strain-rate dependent materials have been studied by Tzavaras ([24, 25]). In this paper we restrict our attention to Newtonian fluids, i.e., $n = 1$ in (4), but note that our qualitative results generalize to $n > 1$.

To complete the model, we impose the boundary conditions

$$v(0, t) = 0 \quad \text{and} \quad v(1, t) = V, \quad t \geq 0,$$

where $V > 0$ is constant since the fluid is subject to a steady shear. We also impose initial conditions $v(x, 0) = v_0(x)$ and $\theta(x, 0) = \theta_0(x)$. Putting this all together, the model problem is

$$\begin{aligned}
v_t(x, t) &= \sigma_x(x, t), & 0 &< x < 1, 0 < t, \\
\theta_t(x, t) &= \sigma(x, t)v_x(x, t), & 0 &< x < 1, 0 < t, \\
v(0, t) &= 0, \ v(1, t) = V, & 0 &< t, \\
v(x, 0) &= v_0(x), \ \theta(x, 0) = \theta_0(x), & 0 &< x < 1,
\end{aligned} \tag{5}$$

where $\sigma(x, t) = \mu(\theta(x, t))v_x(x, t)$.

A short inspection yields two important facts about (5). First, the boundary conditions imply that there is a conserved quantity for the solutions of (5), namely

$$V = v(1) - v(0) = \int_0^1 v_x(s, t)\, ds = \int_0^1 \frac{\sigma(s, t)}{\mu(\theta(s, t))}\, ds. \tag{6}$$

It turns out that this conserved quantity plays a critical role in the large-time behavior of the solutions.

Second, when $v_0(x) = Vx$ and $\theta_0(x) = a$, where $a > 0$ constant, then the solution to (5) is the *uniform shear flow*

$$v(x, t) = Vx, \quad \theta(x, t) = h(t),$$

where $h(t)$ is determined by

$$\int_a^{h(t)} \frac{ds}{\mu(s)} = V^2 t,$$

assuming μ^{-1} is integrable; see Fig. 1. In other words, the flow keeps the uniform shear profile if it begins with a uniform profile. Much of the analysis of (5) in the literature concentrates on understanding the stability of the uniform shear flow, what happens when the initial data $v_0(x)$ are close to $v_0(x) = Vx$ for $V \approx 1$ and θ_0 is close to a positive constant.

As the material is being sheared, energy is pumped into the system. Since the flow is adiabatic, temperature will keep rising and tend to infinity with time. The distribution of temperature can either go to infinity uniformly in space or it could localize. Note that in the uniform shear flow, the temperature grows with t uniformly in x. If the temperature tends to infinity in a localized region in x, then a shear layer can develop in the same region. Shear layers, or bands, are narrow regions in which the velocity of the fluid changes sharply or narrow layers of concentrated shearing deformation are observed during the plastic shearing of materials.

Various mechanisms and associated continuum thermomechanics models have been proposed for the explanation of shear layers and there is extensive literature on the formation of shear layers; see, for example, Bai and Dodd [1], Batra [2, 3], Bayliss *et al.* [5], Clifton *et al.* [8], DiLellio and Olmstead [12, 13], Edwards and French [15], Maddocks and Malek-Madani [20], Needleman [21], Wright [27, 28], and Wright and Walter [29, 30]. For numerical computations of shear layers in various models, we refer to Batra and Ko [4], Drew and Flaherty [14], French and Garcia [19], French [18], and Walter [26].

Many of these references study (5) or closely related models. The motivation for studying this simple model is to obtain a better understanding of the phenomenon of localization of the temperature and the formation of shear layers. Moreover, the conservation laws that define (5) lie at the heart of any more sophisticated models describing shear layer phenomena. The main question we address in this paper is whether or not this simplified model is still sufficiently complex as to allow the formation of shear layers.

Detailed mathematical analyses of (5) have been carried out by Dafermos and Hsiao ([10]), Tzavaras ([23]), and Bertsch *et al.* ([6]). The analysis shows that if $\mu(\theta)$ tends monotonically to a positive constant as $\theta \to \infty$ and either μ^2 is concave or μ is convex, then for all smooth initial data, there is a unique solution of (5) that converges to the uniform shear flow as $t \to \infty$. In other words, the uniform shear flow is a stable solution attracting all smooth solutions. The analysis also shows that the situation is more delicate if the viscosity tends to zero as temperature increases; i.e., $\mu \to 0$ as $\theta \to \infty$. In this case, the existence of solutions and the stability of the uniform shearing flow depend on the rate of decrease of μ with θ. In particular, Dafermos and Hsiao and Bertsch *et al.* consider the test problem (5) when

$$\mu(\theta) = \theta^{-\alpha}, \quad \alpha > 0. \tag{7}$$

The parameter α controls the rate of decrease of the viscosity as the temperature increases. The results can be summarized as follows.

THEOREM 1.1.   1. *If* $0 < \alpha < 1$, *then* (5) *has a unique solution for all time that converges asymptotically to the uniform shear flow as* $t \to \infty$. *In particular,*

$$v_x(x, t) = V + \mathbf{O}\left(t^{-(1-\alpha)/(1+\alpha)}\right)$$

$$\theta(x, t) = \left((1+\alpha)V^2 t\right)^{1/(1+\alpha)} \left(1 + \mathbf{O}\left(t^{-(1-\alpha)/(1+\alpha)}\right)\right). \tag{8}$$

2. *If $\alpha = 1$, then (5) has a unique solution for all time and the gradient of the velocity converges to a steady-state function determined by the initial data while the temperature grows like $\mathbf{O}(t^{1/2})$. In particular, there is a positive function θ^* determined by the initial data such that*

$$\lim_{t \to \infty} v_x(x, t) = \frac{V}{\sqrt{2}} \theta^*(x)$$

$$\lim_{t \to \infty} t^{-1/2}\theta(x, t) = \theta^*(x) \tag{9}$$

$$\sigma(x, t) = \frac{V}{\sqrt{2}} \left(t^{-1/2} + \mathbf{O}(t^{-1}) \right).$$

3. *If $\alpha > 1$ and the initial data are close to the uniform shear flow, then there is a unique solution that moves away from the uniform shear flow and might blow up in finite time.*

Since shear bands do not form in (5) when $\alpha \le 1$, we focus our attention on the case $\alpha > 1$. Aside from the local existence of a unique solution that moves away from the uniform shear flow, not much is known in the case $\alpha > 1$. In particular, it is an open problem whether there exist globally defined smooth solutions. Since pure analysis appears to be extremely delicate, we study this problem using a combination of analytical and numerical methods.

We illustrate the possible behavior in the stable cases $\alpha = 0.5$ and $\alpha = 1$ with a couple of numerical solutions. In both cases, we form initial data for the solutions by perturbing the uniform shear slightly by a small "bump" centered at $x = 0.7$. These initial data correspond to introducing a small amplitude, wide shear layer in v. See Fig. 2. In Fig. 3, we plot a numerical solution for $\alpha = 0.5$. The stability of the uniform shear is evident, although note that θ is not constrained to remain uniform in space. In general, it is difficult to obtain accurate numerical solutions of (4) and we discuss details of our computational method below. As a partial validation of our numerical technique, we verify the estimates on v_x and θ in (7). In Fig. 4, we plot (maximum of $v_x - V)t^{1/3}$ and (maximum of $\theta)t^{-2/3}$ versus time computed from the numerical solution shown in Fig. 3. These plots suggest that the estimates in (7) are indeed precise. Using a least squares line fit, we find that maximum of $v_x - V$ decreases like $t^{-0.335}$ with a correlation in excess of 0.9999 and the maximum of θ increases like $t^{0.666}$ with a correlation in excess of 0.99999. The theoretical values for the rates are $-1/3$ and $2/3$, respectively.

When $\alpha = 1$, the slight perturbation to the shear profile remains fixed as time passes; see Fig. 5. To emphasize the degree to which v_x remains fixed, we plot the initial and final
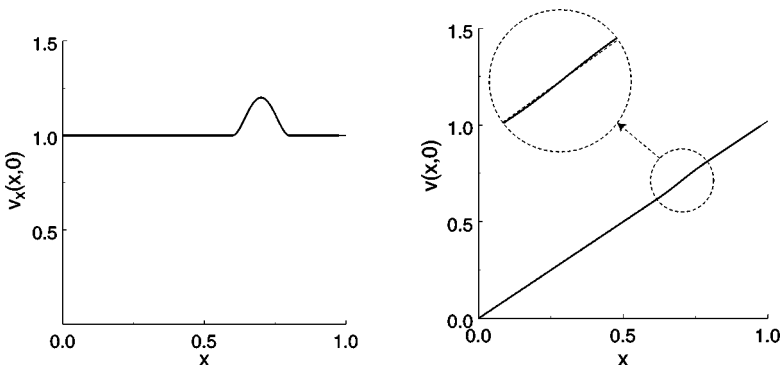

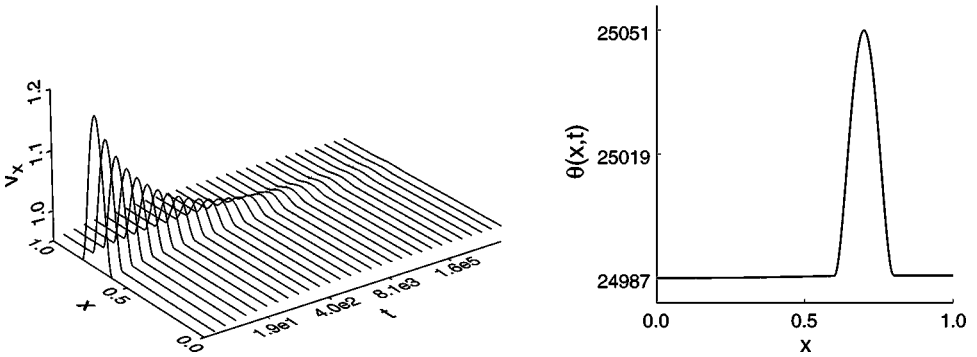**FIG. 2.** Plots of the initial data for v_x and v used for the computation shown in Fig. 3.

FIG. 3. Plots of the evolution of v_x versus time and θ at $t \approx 2500000$ with $\alpha = 0.5$. Initially, v_x and θ have the value 1 perturbed by a smooth bump of height 0.2 and width 0.2 centered at $x = 0.7$.

profiles in Fig. 6. The perturbation initially present in θ grows; see Fig. 6. Thus there is some degree of localization and while the uniform shear flow does not attract solutions, there is a stable attracting profile close to the uniform shear flow (but no smoothing of the solution).

In both cases $\alpha = 0.5$ and $\alpha = 1$, other smooth perturbations in the initial data yield the same qualitative behavior. The only significant difference is that the time scale for v to converge to a steady state is altered.

The behavior of numerical solutions for $\alpha > 1$ is much different than in the stable case of $\alpha \leq 1$. In Fig. 7, we show the evolution of a numerical solution for $\alpha = 2$ starting with the same slight perturbation of the uniform shear flow shown in Fig. 2. A sharp shear layer in the flow is clearly developing. In Fig. 8, we show the evolution of θ and a plot of the maximum value of v_x in x versus t. The plot of the maximum of v_x versus t suggests that the peak height of v_x grows at an exponential rate with t after an initial transient period passes. This corresponds to the shear layer approaching a discontinuous profile at $t = \infty$. The temperature θ is growing uniformly in x but grows much faster at the peak.

In this paper, we investigate (5) under the assumption (7) with $\alpha > 1$ using a combination of numerical and analytical tools. Our results suggest that generic solutions of (5) that begin
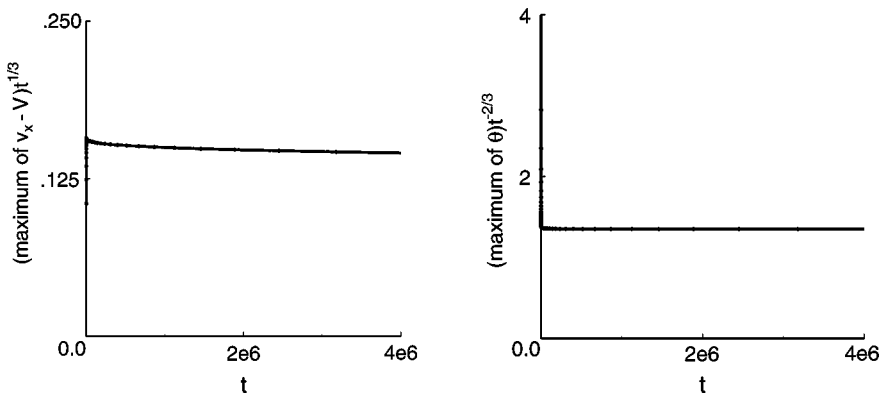

FIG. 4. Plots of (maximum of $v_x - V)t^{1/3}$ and (maximum of $\theta)t^{-2/3}$ versus time computed from the numerical solution shown in Fig. 3.

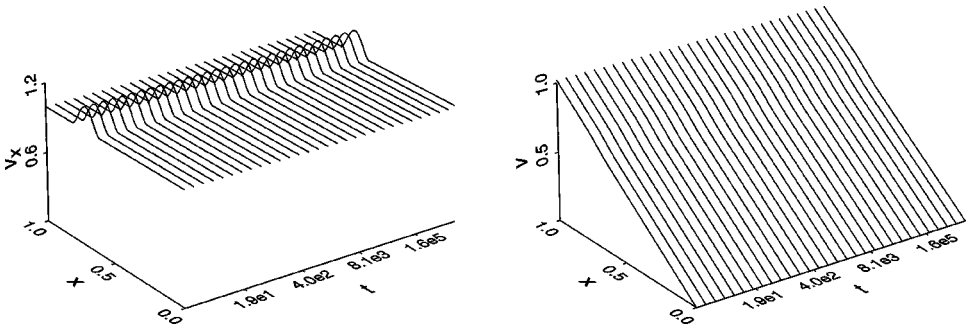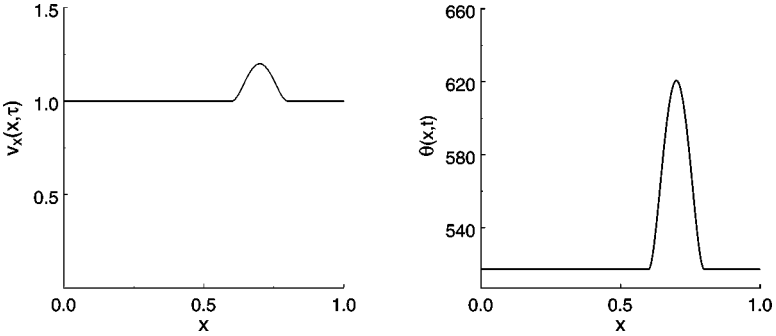**FIG. 5.** Plot of the evolution of v_x and v versus x when $\alpha = 1$. The initial data are shown in Fig. 2.

FIG. 6. Plots of v_x versus x at $t = 0$ and $t \approx 130000$ and θ at $t \approx 130000$ with $\alpha = 1$. The plots of v_x at the two times are indistinguishable.
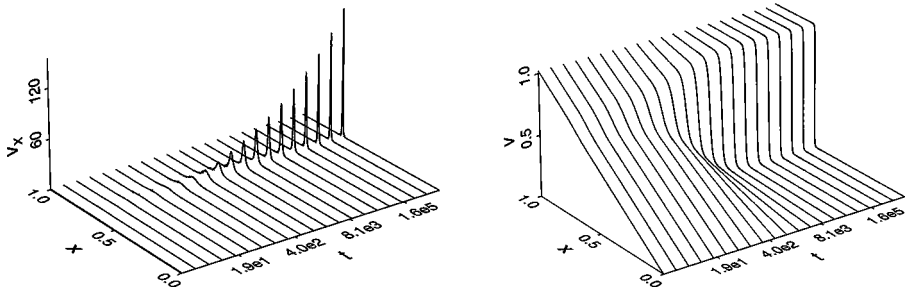

FIG. 7. Plots of the evolution of v_x versus time and the evolution of v versus time with $\alpha = 2$. The initial data are shown in Fig. 2.
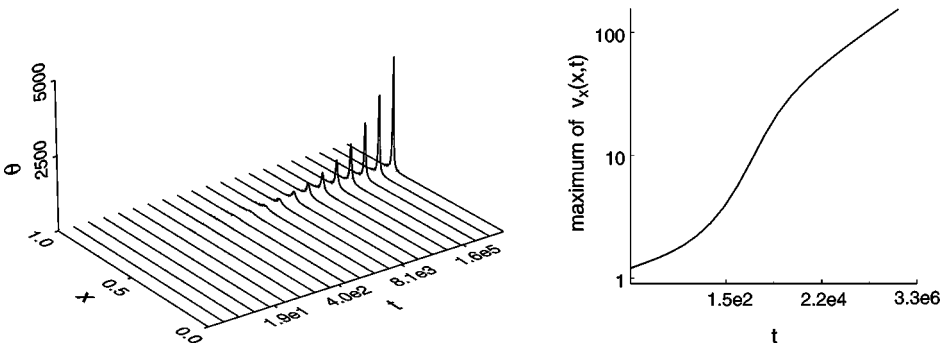

FIG. 8. Plots of the evolution of θ versus time and $\max_x v_x(\cdot, x)$ versus time corresponding to the solution shown in Fig. 7. The vertical axis of the plot on the right is logarithmic.

as smooth perturbations of the uniform shear flow exist for all time but form shear layers that become arbitrarily sharp as time passes. While the formation of layers is unstable behavior, the layers have a kind of structural stability in the sense that data representing nearby perturbations of the same function produce shear layers in the same location and of the same shape and size. We propose a model for the layers which fits the observed behavior very well and use the model to explain some aspects of the behavior of the solutions.

The results shown in Figs. 7 and 8 point to the numerical and analytical difficulties encountered in a study of (5). Particular problems are the multiscale nature of sharp shear layers, the long-time transient to the formation of shear layers, and the apparent loss of regularity, or "blow-up," in the solutions at infinity. We counter these difficulties by first introducing new unknowns and a time variable, which has the effect of changing (5) into a system of reaction–diffusion equations, where the interesting behavior occurs on a more reasonable time scale and the regularity of the solutions is better understood. We then construct a numerical method with special stability properties and use a posteriori error estimates to adaptively control the error by mesh refinement.

In Section 2, we use an equivalent formulation of the original problem (5) using the shear stress and the temperature as basic variables. This leads to a system of reaction–diffusion equations which is more amenable to mathematical and numerical analysis. In Section 3, we present a description of the adaptive finite element method we use to compute solutions, giving some details of special stability properties built into the method. We also justify the use of adaptive mesh refinement and describe the adaptive error control briefly. With the tools developed in these two sections, we are then in a position to be able to attack the problem. We begin in Section 4 by computing a model function that satisfies the differential equation to within a very small residual by an iterative process in which we successively correct the residuals to obtain increasingly accurate approximate solutions. Using numerics, we show that the model function is very close to being a true solution. We also present evidence that a solution that begins as an arbitrary smooth perturbation to the shear flow converges to the model function in the limit of large time. This sets up the theme of Section 5, in which we investigate the convergence of solutions to the model function. In particular, we consider a systematic sequence of initial data and use least squares line fitting to compare each solution obtained to the corresponding model solution. The evidence suggests that solutions that begin as smooth perturbations of the uniform shear flow converge to the model function. Then in Section 6, we widen the investigation of numerical solutions to consider more exotic initial data and also changes to the model in the form of varying α or adding a diffusion term to the original equations. We present evidence that suggests that the phenomena we observe in previous sections are robust with respect to altering the model and we also uncover some interesting and unexplained new behavior. Finally in Section 7, we summarize our results.

2. A REFORMULATION OF THE PROBLEM

The first step in the analysis of (5) is to reformulate the problem in order to make sophisticated analytical and numerical methods available. We describe and motivate the reformulation in this section.

The reformulation has two steps. First we replace (5) for the velocity v and temperature θ by an equivalent system of reaction–diffusion equations for the shear σ and the temperature θ. There are two reasons. First, the results in Fig. 2 suggest that v_x blows up at

infinity when $\alpha > 1$. We can expect such loss of regularity to have a strongly negative effect on the approximation properties of a numerical scheme. Dealing with this negative effect is complicated by the fact that it is indirect unless we explicitly set out to approximate the derivatives of the solution. In contrast using the shear $\sigma = \theta^{-\alpha} v_x$ means that we approximate v_x directly. This has the consequence that the criteria we use to adaptively refine the mesh automatically add mesh points in regions where v_x becomes large. The second reason for changing the problem into a reaction–diffusion system is that the theories for analysis and numerical approximation of reaction–diffusion systems are both well developed, giving many useful tools. In particular, we use the ideas of invariant regions and comparison principles (see Chueh *et al.* [7] and Smoller [22]) and the theory of a posteriori error estimation and adaptive error control for finite element methods (see Estep *et al.* [16]).

Differentiating $\sigma = \theta^{-\alpha} v_x$ and substituting it into the equation for v in (5) yields a system of degenerate reaction–diffusion equations

$$\sigma_t - \theta^{-\alpha}\sigma_{xx} = -\alpha\theta^{\alpha-1}\sigma^3, \quad 0 < x < 1, \ 0 < t,$$
$$\theta_t = \theta^\alpha\sigma^2, \quad\quad\quad 0 < x < 1, \ 0 < t, \tag{10}$$

with boundary conditions and initial data given by

$$\sigma_x(0, t) = \sigma_x(1, t) = 0, \quad\quad\quad 0 < t,$$
$$\sigma(x, 0) = \sigma_0(x), \ \theta(x, 0) = \theta_0(x), \quad 0 < x < 1, \tag{11}$$

In the second step of the reformulation of (5), we attempt to account for the natural increase in temperature due to the assumption of an adiabatic process and to the long time scales observed in the computed solutions. To find the natural time scale in the system, we first neglect the variation in space and consider the resulting system of ordinary differential equations

$$\sigma_t = -\alpha\theta^{\alpha-1}\sigma^3,$$
$$\theta_t = \theta^\alpha\sigma^2. \tag{12}$$

Separating variables, we find that $\sigma_t/\sigma = -\alpha\theta_t/\theta$ or $\sigma = \hat{c}\theta^{-\alpha}$. Substituting this into the equation for θ and solving, we obtain

$$\theta(t) = ((\alpha + 1)\hat{c}^2 t)^{1/(1+\alpha)} \quad \text{and} \quad \sigma(t) = \hat{c}((\alpha + 1)\hat{c}^2 t)^{-\alpha/(1+\alpha)}.$$

This suggests that we rescale the stress and temperature as

$$\tilde{s}(x, t) = (t + 1)^{\alpha/(1+\alpha)}\sigma(x, t), \quad \tilde{r}(x, t) = (t + 1)^{-1/(1+\alpha)}\theta(x, t). \tag{13}$$

In addition, we change to a logarithmic time scale by setting $\tau = \log(t + 1)$. With $r(\cdot, \tau) = \tilde{r}(\cdot, e^\tau - 1)$ and $s(\cdot, \tau) = \tilde{s}(\cdot, e^\tau - 1)$, the functions r and s solve the problem

$$s_\tau - r^{-\alpha}e^{\tau/(1+\alpha)}s_{xx} = \frac{\alpha}{1+\alpha}s(1 - (\alpha + 1)r^{\alpha-1}s^2), \quad 0 < x < 1, \ 0 < \tau,$$
$$r_\tau = -\frac{1}{1+\alpha}r(1 - (\alpha + 1)r^{\alpha-1}s^2), \quad 0 < x < 1, \ 0 < \tau. \tag{14}$$

The corresponding boundary and initial data become

$$s_x(0, \tau) = s_x(1, \tau) = 0, \qquad\qquad 0 < \tau,$$
$$s(x, 0) = s_0(x), \; r(x, 0) = r_0(x), \quad 0 < x < 1. \tag{15}$$

Note that $s_0(x) = \sigma_0(x)$ and $r_0(x) = \theta_0(x)$.

To see that the variables r and s are natural for this problem when $\alpha \le 1$, we use the concept of invariant regions. An invariant region for a system of differential equations is a region in phase space with the property that a solution that begins with data inside the region remains inside for all time. The existence of a compact invariant region for a system of reaction–diffusion equations has strong consequences such as global existence and smoothness of solutions. See Smoller [22] for a detailed discussion.

In general, it can be difficult to find an invariant region for a system of equations. However, it is often easier to find a special kind of invariant region called an invariant rectangle, which is an invariant region consisting of a generalized rectangle in phase space with sides parallel to the coordinate planes. There is a simple geometric condition that guarantees that a rectangle is invariant for a system of the form (14) which is that the reaction term points inward on each face of the rectangle. In fact, a common way of demonstrating the existence of a compact invariant region for a given system is to find new variables in which the corresponding problem has an invariant rectangle.

We plot the phase fields for (14) in the cases $\alpha = 0.5, \alpha = 1$, and $\alpha = 2$ in Fig. 9. We can find many invariant rectangles in the case $\alpha = 0.5$ and many invariant "strips" when $\alpha = 1$.

On the other hand, there is no apparent invariant region bounded away from the coordinate axes when $\alpha = 2$. In fact, the numerical evidence for the formation of arbitrarily sharp shear layers when $\alpha > 1$ suggests that there cannot be an invariant region for the solution when $\alpha > 1$. In Fig. 10, we show the evolution of s and r corresponding to the computations shown in Figs. 7 and 8 for σ and θ. The formation of a shear layer corresponds to blow up in r in the form of a sharp, highly localized peak that grows with τ.

We can devise a partial explanation of the observed behavior in r and s after realizing there is a conserved integral quantity involving r and s. Indeed, (6) implies that

$$\int_0^1 s(\cdot, x) r^\alpha(\cdot, x) \, dx = \int_0^1 \sigma(\cdot, x) \theta^\alpha(\cdot, x) \, dx = \int_0^1 v_x(\cdot, x) \, dx = V. \tag{16}$$
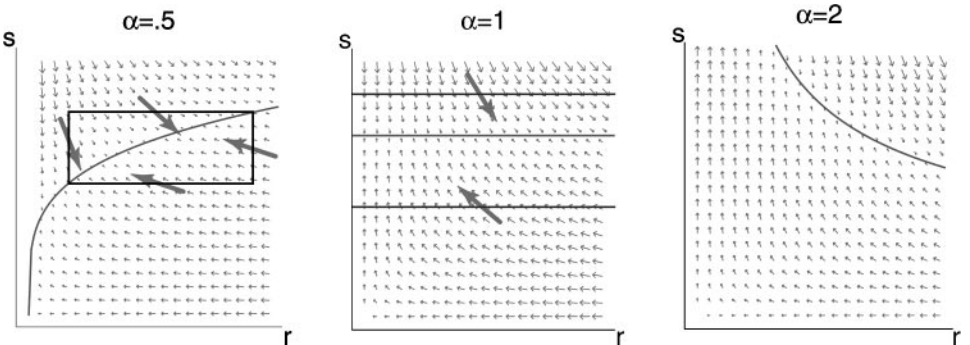

FIG. 9. Plots of the phase fields for (13) in the cases $\alpha = 0.5, \alpha = 1$, and $\alpha = 2$. Both zero level contours and the boundaries of the invariant regions are drawn.
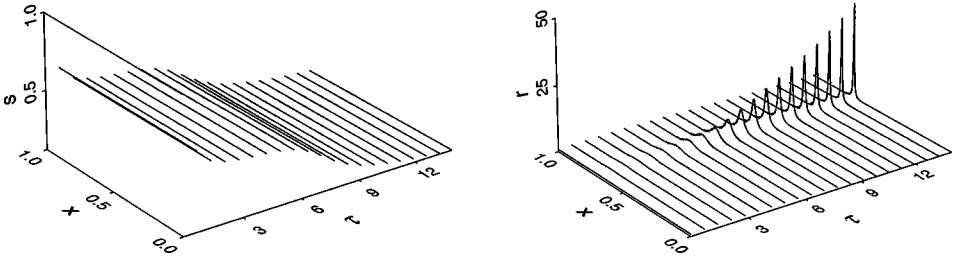
FIG. 10. Plots of the evolution of s and r versus time corresponding to the computations shown in Fig. 7.

If s were independent of the spatial variable, as in the ordinary differential equation model, the conserved quantity would imply that a sharp peak in r must become more localized as the peak grows in height while away from the peak, r would have to tend to zero. We plot r at $\tau \approx 14$ in Fig. 11.

However, though nearly flat, s in fact is not constant in x; see Fig. 11. In regions where r becomes small, the diffusion in the equation for s becomes large and consequently s is relatively constant in x. However, in a narrow region near the peak of r, the diffusion in the equation for s is extremely close to zero allowing for an extreme degree of localization in the spatial profile of s. Correspondingly, the effect of the growth of a narrow peak in r on the conserved quantity is partly compensated by the behavior in s. This small lack of uniformity and smoothness in the space behavior of s, when $\alpha > 1$, turns out to be crucial to the observed behavior of r and s as well as the crux in the analysis of the problem.

3. THE NUMERICAL METHOD

There are several particular concerns when constructing a numerical method for (14) in view of the formation of shear layers. First, there is an issue of accuracy arising from the extreme multiscale behavior associated with sharp shear layers. Second, the formation of shear layers takes place after a significantly long transient time. Third, the formation of shear layers is associated with blow-up in the solutions at infinity. The goal can be summarized as creating a numerical method that maintains accuracy during the onset of blow-up while avoiding the introduction of artificial, or numerical, instabilities.

We employ a finite element method in which the error is controlled via adaptive mesh refinement. The refinement is controlled by means of an a posteriori error estimate in
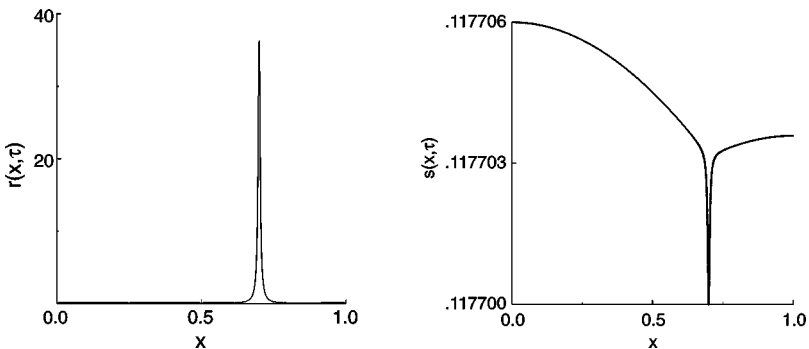

FIG. 11. Plots r and s at $\tau \approx 14$ corresponding to the computation shown in Fig. 10.
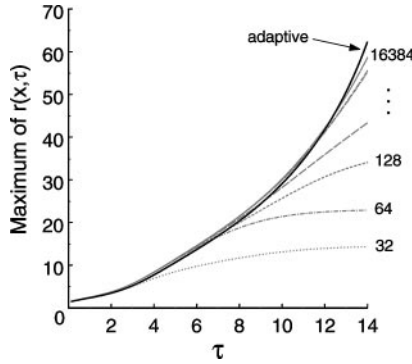
FIG. 12. Plot of the peak height of r versus τ for a series of fixed mesh computations using $m = 32, 64, \ldots, 16000$ nodes and one adaptive mesh computation denoted by the solid line starting with the initial data used in the computation shown in Fig. 10. The adaptive computation is using 8192 elements at $\tau = 14$.

which the error is measured in terms of properties of the numerical solution. This control avoids strong assumptions or knowledge about the regularity of the solution that cannot be verified in this problem. Since adaptive methods are relatively complicated to implement, we motivate the use for computing solutions of (14) using an experiment. We compute numerical solutions of (14) with the initial data used in the computation shown in Fig. 10 using fixed meshes with $m = 32, 64, \ldots$, up to 16,384 elements and one solution using the adaptive strategy (described in detail below). In Fig. 12, we plot the peak height of r measured from the numerical approximation of r versus τ for each computation. When a fixed mesh is used, the peak height of r invariably stops growing after the "tip" of the peak becomes narrower than the mesh spacing; hence we find that the maximum peak height depends on h, which can be seen clearly in the plot. On the other hand, the peak height of f measured from the adaptive computation indicates an unbounded exponential growth rate in τ. We believe the adaptive computation is much more accurate than any of the computations on the fixed mesh, while only 8192 elements are used at the end of the adaptive computation shown in Fig. 12.

However, using adaptive meshing to solve a problem exhibiting "blow-up" raises an issue of numerical stability. In effect, mesh refinement can put "energy" into the system and thus be a source of artificial "blow-up." This happens, for example, if the numerical method has some instability that affects the error estimator which in turn calls for mesh refinement that can further drive the instability. To avoid this, we construct a finite element method that has several special stability properties. For one thing, the method preserves a discrete version of the conserved quantity (16). As we have seen, the conserved quantity plays an essential role in determining the blow-up profile. It also provides a measure of the accuracy of the numerical solution over time. Another stability property of the finite element method is that for a general class of reaction–diffusion systems, it exactly preserves invariant rectangles for all sufficiently small time steps. Moreover, the adaptive error control we employ guarantees that the numerical method approximately preserves invariant regions for a larger class of reaction–diffusion systems. We give details of these properties below. For now, we note that the plot in Fig. 12 suggests that at any fixed τ the peak heights of r computed on the uniform meshes converge to the peak height obtained with the adaptive computation as the number of elements increases. Moreover we obtain virtually indistinguishable plots of the peak height of r from adaptive computations corresponding to all error tolerances smaller than a critical value (which is relatively large).

The finite element method is a variation of the space–time, discontinuous Galerkin (dG), finite element method. We describe the method and some results briefly and refer to Estep *et al.* [16, 17] for more details on the method and the a posteriori error analysis.

We partition $[0, \infty)$ as $0 = \tau_0 < \tau_1 < \tau_2 < \cdots < \tau_n < \cdots$, denoting each τ interval by $I_n = (\tau_{n-1}, \tau_n)$ and τ-step by $k_n = \tau_n - \tau_{n-1}$. To each interval I_n, we associate a partition $\mathcal{T}_n$ of $(0, 1)$ described by nodes $x_{n,0} = 0 < x_{n,1} < \cdots x_{n,m_n+1} = 1$ with mesh sizes $h_{n,i} = x_{n,i} - x_{n,i-1}$. Note that mesh changes are allowed across τ nodes.

The approximation is a discontinuous constant polynomial in τ and a continuous, piecewise linear polynomial in space on each space-τ "slab" $S_n = (0, 1) \times I_n$. In space, we let $V_n \subset H^1(0, 1) \times H^1(0, 1)$ denote the space of piecewise, linear, continuous vector-valued functions $v(x) = (v_1, v_2)^\top$ defined on $\mathcal{T}_n$. Then on each slab, we define

$$W_n^0 = \{w(x, \tau) : w(x, \tau) = v^n(x), \ v^n \in V_n, \ (x, \tau) \in S_n\}.$$

Finally, we let W^0 denote the space of functions defined on the space-τ domain $(0, 1) \times \mathbf{R}^+$ such that $v|_{S_n} \in W_n^0$ for $n \geq 1$. Note that functions in W^0 are generally discontinuous across the discrete τ levels and we denote the jump across τ_n by $[w]_n = w^n - w^{n-1}$.

In order to construct a method that preserves the integral quantity in a discrete sense, we change variables to replace r by $\hat{r} = r^\alpha$. All of our results are presented in terms of the original r. The problem (14) is changed to

$$s_\tau - \hat{r}^{-1} e^{\tau/(1+\alpha)} s_{xx} = \frac{\alpha}{1 + \alpha} s \left(1 - (\alpha + 1)\hat{r}^{(\alpha-1)/\alpha} s^2\right), \qquad 0 < x < 1, \ 0 < \tau,$$
$$\hat{r}_\tau = -\frac{\alpha}{1 + \alpha} \hat{r} \left(1 - (\alpha + 1)\hat{r}^{(\alpha-1)/\alpha} s^2\right), \quad 0 < x < 1, \ 0 < \tau, \tag{17}$$

with boundary and initial data

$$s_x(0, \tau) = s_x(1, \tau) = 0, \qquad\qquad 0 < \tau,$$
$$s(x, 0) = s_0(x), \ \hat{r}(x, 0) = r_0(x)^\alpha, \quad 0 < x < 1. \tag{18}$$

To simplify the notation, we let $u = (u_1, u_2) = (s, \hat{r})^\top$ and write the variational formulation of (17) as $u \in L^2(H^1(0, 1) \times H^1(0, 1))$ such that

$$\int_0^\tau (u_\tau, v) \, d\tau + \int_0^\tau (u_x, (D(u, \tau)v)_x) \, d\tau = \int_0^\tau (f(u), v) \, d\tau$$

for all $v \in L^2(H^1(0, 1) \times H^1(0, 1))$ with $u(\cdot, 0) = u^0 = (s_0, r_0^\alpha)^\top$, where $L^2(H^1(0, 1) \times H^1(0, 1))$ denotes functions that are L^2 in τ and H^1 in x, $(,)$ denotes the $L_2(0, 1)$ inner product with corresponding norm $\| \ \|$, and

$$D(u, \tau) = \begin{pmatrix} e^{\tau/(1+\alpha)} u_2^{-1} & 0 \\ 0 & 0 \end{pmatrix}, \quad f(u) = \begin{pmatrix} u_1\left(\frac{\alpha}{1+\alpha} - \alpha u_2^{(\alpha-1)/\alpha} u_1^2\right) \\ -u_2\left(\frac{\alpha}{1+\alpha} - \alpha u_2^{(\alpha-1)/\alpha} u_1^2\right) \end{pmatrix}.$$

Note we are simply assuming that u lies in the indicated space of course. The discontinuous Galerkin method reads: compute $U \in W^0$ such that for $n \geq 1$,

$$\int_{I_n} (U_\tau, v) \, d\tau + \int_{I_n} (U_x, (D(U, \tau)v)_x) \, d\tau + ([U]_n, v) = \int_{I_n} (f(U), v) \, d\tau$$

for all $v \in V_n$ and $U(\cdot, 0) = U^0 \approx u^0$ is a suitable approximation of the initial data.

As can be seen, the discontinuous Galerkin method is an implicit method in τ requiring the solution of a system of nonlinear equations on each τ interval. However, we are computing solutions of (14) that are not very smooth and therefore the τ steps have to be kept small for the sake of accuracy, negating any possible gain in efficiency from using large τ steps in a nonlinear discretization. Thus, we modify the standard discontinuous Galerkin method to construct a semiimplicit method. The modifications are obtained by introducing an extrapolation operator and numeric quadrature in the variational formulation of (14).

To make the discretization semiimplicit, we use the extrapolation operator $\mathcal{P}$ defined on $U \in W^0$ by $\mathcal{P}U|_{I_n} = P_n U^{n-1}$ for $n \geq 1$, where P_n denotes an interpolation operator into V_n. (To maintain smooth profiles near the "tip" of the peak in r, we define P_n using local averaging.) We also write f as $f(u) = f_e(u)u + f_i(u)u$ for diagonal matrices

$$f_e(u) = \begin{pmatrix} 0 & 0 \\ 0 & -\frac{\alpha}{1+\alpha} + \alpha u_2^{(\alpha-1)/\alpha} u_1^2 \end{pmatrix} \quad \text{and} \quad f_i(u) = \begin{pmatrix} \frac{\alpha}{1+\alpha} - \alpha u_2^{(\alpha-1)/\alpha} u_1^2 & 0 \\ 0 & 0 \end{pmatrix}.$$

The semiimplicit method is found by computing $U \in W^0$ satisfying

$$\int_{I_n} (U_\tau, v)\, d\tau + \int_{I_n} (U_x, (D(\mathcal{P}U, \tau)v)_x)\, d\tau + ([U]_n, v) - \int_{I_n} (f_i(\mathcal{P}U)U, v)\, d\tau$$
$$= \int_{I_n} (f_e(\mathcal{P}U)\mathcal{P}U, v)\, d\tau,$$

for all $v \in V_n$. As the final step in the discretization, we use quadrature to evaluate some of the integrals in this equation. Since we expect first-order convergence in τ and second-order in x, we use the rectangle rule to evaluate the integrals in τ with the right-hand endpoint of I_n and the trapezoidal, or lumped mass, quadrature rule to evaluate the last three space integrals. We compute the space integral for the diffusion term exactly. Noting that $U_\tau \equiv 0$, we get that $U^n \in V_n$ satisfies

$$\left(U_x^n, (D(P_n U^{n-1}, \tau)v)_x\right) k_n + \langle U^n, v \rangle - \left\langle f_i(P_n U^{n-1})U^n, v \right\rangle k_n$$
$$= \langle U^{n-1}, v \rangle + \left\langle f_e(P_n U^{n-1})P_n U^{n-1}, v \right\rangle k_n, \tag{19}$$

for all $v \in V_n$, where $\langle\,,\,\rangle$ denotes the lumped mass L^2 inner product on functions in V_n. Equation (19) yields a linear tridiagonal system that we solve with a direct method.

Combining the dG method with the rectangle rule to compute integrals in time and the lumped mass quadrature rule to evaluate integrals in space yields a method with strong stability properties. In particular when applied to a system of nonsingular reaction–diffusion equations with constant diffusion in which the solution is converging to a steady state, the approximation converges to the same steady state. In general for such systems, the method exactly preserves any invariant rectangles that exist for the continuous system under a CFL-like condition on the time steps.

The choice of τ steps and space meshes is based on an a posteriori estimate of the error of U. We refer to Estep *et al.* [16] for details of the a posteriori error analysis and its use for computational error estimation and adaptive mesh refinement. The quality of the discretization is measured locally in terms of the residual $\mathcal{R}$, which is obtained by substituting U into the (weak form of the) differential equation. The residual measures show how well the numerical solution satisfies the differential equation at each point. The
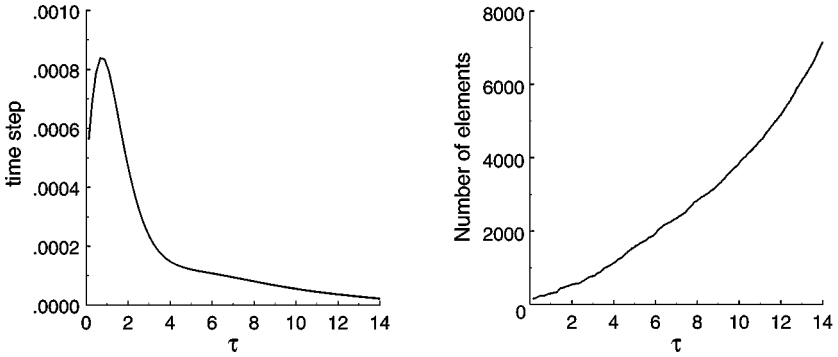
FIG. 13. Plots of the τ steps and number of mesh nodes for the adaptive computation in Fig. 12 versus τ.

true solution has residual equal to zero, of course. The error e of U is related to the residual of U using a variational analysis that involves the dual problem to the original problem (14). The estimate takes the form

$$\|e(\cdot, \tau)\| \leq S(\tau) \max_{0 \leq s \leq \tau} \|\mathcal{R}(\cdot, s)\| \tag{20}$$

for $\tau \geq 0$. $S(\tau)$ is called the stability factor and reflects the stability of the solution up to τ. The stability factor plays the role of a condition number of a matrix in the solution of a linear system. To obtain an error bound, we can bound $S(\tau)$ using properties such as well-posedness. Typically, such bounds grow exponentially in τ. In most problems in practice, $S(\tau)$ is estimated computationally by solving the dual problem numerically because long τ exponential growth is not observed. However, in the case of (14) the computed stability factor grows at a steady slow exponential rate. In this situation, it is reasonable to control the error by equidistributing the local contributions to the residual of U from each interval. To illustrate how the adaptivity works, in Fig. 13 we plot the τ steps and number of elements versus τ used for the computation with $\alpha = 2$ shown in Fig. 12. We also show the adapted mesh at $\tau \approx 12$ in Fig. 14. As a partial validation of the consistency of the numerical results, we repeated many of the computations presented in this paper for a range of tolerances on the size of the residual. We found that using tolerances smaller than a (relatively large) critical value leads to consistent numerical results. The computational results presented in this paper correspond to residual tolerances in the range of 10^{-3} to 10^{-4}.
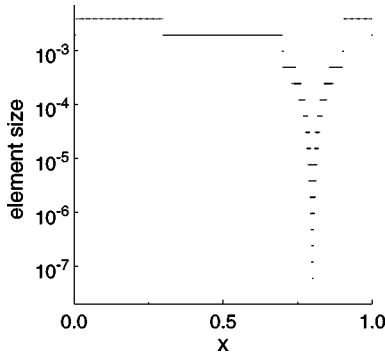

FIG. 14. Plot of the mesh sizes versus x for the adaptive computation at $\tau \approx 12$ for the adaptive computation in Fig. 12.

As mentioned, one advantage gained from this adaptive error control is that it approximately preserves invariant regions. More precisely, it is proved in Estep *et al.* [16] that if there is an invariant rectangle for the true solution of a general system of reaction–diffusion equations, then the numerical solution computed so as to control the residual will remain inside an approximate invariant rectangle. Moreover, the approximate invariant rectangle converges to the true invariant rectangle as the tolerance on the residual is decreased to zero. These are important stability results because they eliminate the possibility of artificial blow-up in the sense that if the true solution does have an invariant rectangle, then for sufficiently small tolerances, we will not observe blow up in the numerical solution—Vice versa if we observe blow up in numerical solutions regardless of the tolerance used in the adaptive error control; this is strong evidence that blow up is occurring.

These stability results depend on the form of the reaction–diffusion system and the numerical method only to the extent that they require certain energy estimates on the approximation. These estimates are the discrete analogs of energy estimates on derivatives of the true solution that can be proved once an invariant rectangle for the true solution has been established. In Estep *et al.* [16], the required estimates are established for dG approximations on a general class of reaction–diffusion equations, but not directly for (14). The analogous continuous estimates can be proved for (14) when $\alpha < 1$, so we conjecture that it is possible to obtain the discrete estimates in this case. We do not believe the continuous estimates hold when $\alpha > 1$. Experimentally, the numerical method appears to preserve the invariant rectangles that exist for the true solution when $\alpha < 1$. In addition, as mentioned, we obtain consistent rates of growth of, for example, the peak height of r for all sufficiently small tolerances.

As mentioned, the finite element solution (19) preserves a discrete version of the conserved quantity (16). In particular, we show that if the space meshes are held constant in τ then

$$\sum_{i=0}^{m+1} U_{1,i}^n U_{2,i}^n = \sum_{i=0}^{m+1} U_{1,i}^{n-1} U_{2,i}^{n-1} \tag{21}$$

for all n, where $m = m_n$. In terms of the original variables, this means that

$$\sum_{i=0}^{m+1} S_i^n \left(R_i^n \right)^\alpha = \sum_{i=0}^{m+1} S_i^{n-1} \left(R_i^{n-1} \right)^\alpha$$

using $S \approx s$ and $R \approx r$ to denote the numerical approximations.

Since the mesh is fixed, we have $P_n U^{n-1} = U^{n-1}$. We decompose (19) into equations for each component

$$\left((U_1^n)_x, \left((U_2^{n-1})^{-1} e^{\tau_n/(1+\alpha)} v \right)_x \right) k_n + \left\langle U_1^n, v \right\rangle$$
$$- \left\langle \left(-\frac{\alpha}{1+\alpha} + \alpha (U_2^{n-1})^{(\alpha-1)/\alpha} (U_1^{n-1})^2 \right) U_1^n, v \right\rangle k_n = \left\langle U_1^{n-1}, v \right\rangle \tag{22}$$

and

$$\left\langle U_2^n, v \right\rangle = \left\langle U_2^{n-1}, v \right\rangle + \left\langle \left(\frac{\alpha}{1+\alpha} - \alpha (U_2^{n-1})^{(\alpha-1)/\alpha} (U_1^{n-1})^2 \right) U_2^n, v \right\rangle k_n. \tag{23}$$

We choose $v = U_2^{n-1}$ in (21) and $v = U_1^n$ in (23) and note that the diffusion term in (22) is zero with this choice. We obtain the equations

$$\langle U_1^n, U_2^{n-1}\rangle = \langle U_1^{n-1}, U_2^{n-1}\rangle - \left\langle \left(\frac{\alpha}{1+\alpha} - \alpha \left(U_2^{n-1}\right)^{(\alpha-1)/\alpha} \left(U_1^{n-1}\right)^2\right) U_1^n, U_2^{n-1}\right\rangle k_n$$

$$\langle U_2^n, U_1^n\rangle = \langle U_2^{n-1}, U_1^n\rangle + \left\langle \left(\frac{\alpha}{1+\alpha} - \alpha \left(U_2^{n-1}\right)^{(\alpha-1)/\alpha} \left(U_1^{n-1}\right)^2\right) U_2^n, U_1^n\right\rangle k_n.$$

Adding these equations gives $\langle U_1^n, U_2^n\rangle = \langle U_1^{n-1}, U_2^{n-1}\rangle$, which is (21).

Mesh refinement leads to a very slow increase in the quantity $\sum_{i=0}^{m+1} U_{1,i}^n U_{2,i}^n$ so the adaptive solution is not exactly conservative. In fact, even without the changes caused by mesh refinement, round-off errors in the computation of U^n also tend to cause increases in the "conserved" quantity. However, both of these increases are extremely small and $\sum_{i=0}^{m+1} U_{1,i}^n U_{2,i}^n$ maintains the same value to 9–10 decimal places for the τ scales of computations used in this paper. On the other hand, if we compute for sufficiently large τ, with a range that depends on the data, then $\sum_{i=0}^{m+1} U_{1,i}^n U_{2,i}^n$ begins to change significantly from the initial value. In general for τ this large, the diffusion in (19) is nearly zero and consequently the system is nearly singular because of the Neumann boundary conditions.

4. A MODEL FOR SOLUTIONS THAT FORM SHEAR LAYERS

In this section, we use a combination of analysis and numerics to identify a special approximate solution that is closely related to solutions that blow up. This approximate solution is almost an exact solution, in the sense that its residual tends to zero as τ tends to infinity. Solutions that blow up apparently tend toward this special approximate solution relatively quickly, so that it characterizes the blow-up profile and the rate of blow-up.

The construction of the approximate solutions is based on the observation that applying variation of parameters to the ordinary differential equation for r in (14) yields a formula for r as a function of s,

$$r(x, \tau) = \frac{e^{-\tau/(1+\alpha)}}{r_0(x)^{-1} - w(x, \tau)}, \tag{24}$$

where w solves

$$w_\tau = e^{-\tau/(1+\alpha)} s^2, \quad w(0, 0) = 0.$$

Note that this implies that

$$r(x, \tau) \geq e^{-\tau/(1+\alpha)} r_0(x) \quad \text{for } 0 < x < 1 \text{ and } 0 < \tau.$$

In other words, r cannot approach zero in finite τ.

The formula for r could be used to eliminate r from the reaction–diffusion equation for s, but the resulting equation is very complicated. Rather than using a direct substitution, we use an iterative procedure. Starting with an Ansatz on the form of the solution s, $s(x, \tau) = s_1(x, \tau)$, we use (24) to compute a corresponding approximation $r_1(x, \tau)$ with initial data
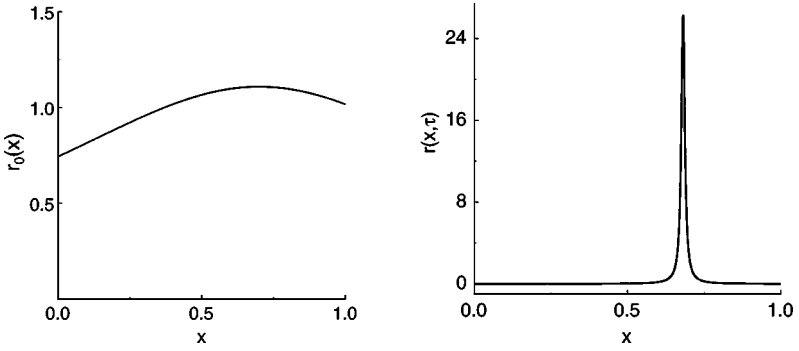
FIG. 15. Plots of the initial data $r_0(x)$ (26) and the numerical solution $r(x, \tau)$ at $\tau \approx 21$.

$r_1(x, 0) = r_0(x)$. The approximation (s_1, r_1) does not satisfy the diffusion equation for s exactly. We compute a correction s_2 to s_1 by solving the following elliptic problem

$$-r_1^2 e^{\tau/3}(s_2)_{xx} = -(s_1)_\tau + \frac{\alpha}{1+\alpha}\left(1 - (\alpha+1)r_1^{\alpha-1}s_1^2\right) + r_1^2 e^{\tau/3}(s_1)_{xx}, \quad 0 < x < 1$$
$$(s_2)_x \approx 0, \qquad\qquad\qquad\qquad\qquad\qquad\qquad\qquad\qquad x = 0, 1. \tag{25}$$

We can then use the corrected approximate solution $s_1 + s_2$ to compute a correction r_2 to r_1 using (24) as above. We can repeat this iteration as long as desired.

The following choice of initial data allows the two-point boundary value problem (24) to be solved exactly

$$\theta_0(x) = r_0(x) = \frac{C_1}{1 + C_2(x - \bar{x})^2} \quad \text{and} \quad \sigma_0(x) = s_0(x) = C_3 \tag{26}$$

while providing a smooth, "bump"-shaped perturbation to the initial uniform shear profile. We plot $r_0(x)$ with $C_1 = 1.108422867$, $C_2 = 1$, $C_3 = 1$, and $\bar{x} = 0.7$ in Fig. 15. We choose the value of C_1 to normalize $r_0(x)$ to have average value 1. We plot the evolution of the corresponding numerical solutions in Fig. 16 and plot $r(x, \tau)$ versus x at $\tau \approx 21$ in Fig. 15.

Based on the numerical solution, we make the Ansatz that the leading order of the solution s be independent of x, i.e., $s(x, \tau) = s_1(\tau)$ with

$$s_1(\tau) = C_3 e^{-\sigma_3 \tau}. \tag{27}$$

Next we solve the differential equation for r with $s(x, \tau) = s_1(\tau)$. The differential equation
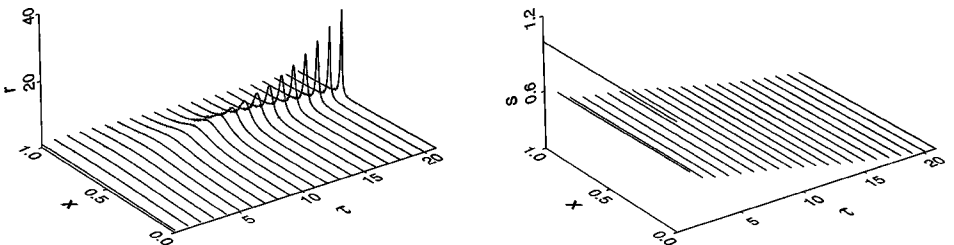

FIG. 16. Plots of the evolution of r and s versus τ starting with the initial data (26).

for w becomes

$$w_\tau(x, \tau) = C_3^2 e^{-((\alpha+1)^{-1}+2\sigma_3)\tau}, \quad w(0, 0) = 0.$$

We define $\sigma_2 = (\alpha + 1)^{-1} + 2\sigma_3$ and integrate the equation to find

$$w(x, \tau) = \frac{C_3^2}{\sigma_2}\left(e^{-\sigma_2\tau} - 1\right).$$

So from (24) it follows that r_1 is given by

$$r_1(x, \tau) = \frac{C_1 e^{-\tau/(\alpha+1)}}{1 + C_2(x - \bar{x})^2 + C_1 C_3^2 \sigma_2^{-1}\left(e^{-\sigma_2\tau} - 1\right)}.$$

If we set $\frac{C_1 C_3^2}{\sigma_2} = \lambda$, then r_1 becomes

$$r_1(x, \tau) = \frac{1}{\lambda}\frac{C_1 e^{\sigma_1\tau}}{1 + \left(\frac{1-\lambda}{\lambda} + C_2(x - \bar{x})^2\right)e^{\sigma_2\tau}}.$$

Now we see that for a peak to develop at $x = \bar{x}$ for r_1, we have to set $\lambda = 1$. So we arrive at the following approximation for r

$$r_1(x, \tau) = \frac{C_1 e^{\sigma_1\tau}}{1 + C_2(x - \bar{x})^2 e^{\sigma_2\tau}}, \tag{28}$$

where

$$\frac{C_1 C_3^2}{\sigma_2} = 1, \quad \sigma_1 = 2\sigma_3 \quad \text{and} \quad \sigma_2 = (\alpha + 1)^{-1} + 2\sigma_3. \tag{29}$$

With this normalization, the functions r_1 and s_1 given by (28) and (27) are an exact solution to the ordinary differential equation

$$(r_1)_\tau = -\frac{1}{\alpha}r_1\left(1 - (\alpha + 1)r_1^{\alpha-1}s_1^2\right).$$

Next we compute the residual of r_1 and s_1 for the equation for s in (14). First note that

$$\frac{(r_1)_\tau}{r_1} = -\frac{1}{\alpha + 1}\left(1 - (\alpha + 1)r_1^{\alpha-1}s_1^2\right)$$

and the residual $R(r_1, s_1)$ for the equation for s in (14) is given by

$$R(r_1, s_1) = (s_1)_\tau - \frac{\alpha}{\alpha + 1}\left(1 - (\alpha + 1)r_1^{\alpha-1}s_1^2\right)$$

$$= (s_1)_\tau + \alpha\frac{s_1}{r_1}(r_1)_\tau.$$

We first compute $(r_1)_\tau$

$$(r_1)_\tau = \frac{2\sigma_3 C_1 e^{\sigma_1\tau}}{1 + C_2(x - \bar{x})^2 e^{\sigma_2\tau}} - \frac{C_1 C_2 \sigma_2(x - \bar{x})^2 e^{\sigma_2\tau}}{\left(1 + C_2(x - \bar{x})^2 e^{\sigma_2\tau}\right)^2}$$

and this leads to the following expression for the residual $R(r_1, s_1)$

$$R(r_1, s_1) = C_3\sigma_3(2\alpha - 1)e^{-\sigma_3\tau} - \frac{\alpha C_1 C_3 \sigma_2 (x - \bar{x})^2 e^{(\sigma_2 - \sigma_3)\tau}}{1 + C_2(x - \bar{x})^2 e^{\sigma_2\tau}}. \tag{30}$$

If $\sigma_3 > 0$, as is suggested by the numerical computation, we see that $R(r_1, s_1)$ tends to zero as τ tends to infinity. So, as $\tau \to \infty$, (r_1, s_1) is a solution of (13).

To compute the second-order term of $s_2(x, \tau)$ of $s(x, \tau)$ we specialize to the case $\alpha = 2$, in which system (14) becomes

$$r_\tau = -\frac{1}{3}r(1 - 3rs^2),$$

$$s_\tau = \frac{2}{3}s(1 - 3rs^2) + r^{-2}e^{\tau/3}s_{xx}. \tag{31}$$

We set

$$s_2(x, \tau) = C_4 \frac{e^{-\sigma_4\tau}}{1 + C_2(x - \bar{x})^2 e^{\sigma_2\tau}}. \tag{32}$$

The first and second derivative of s_2 with respect to x are given by

$$(s_2)_x(x, \tau) = -\frac{2C_2 C_4 (x - \bar{x})e^{(\sigma_2 - \sigma_4)\tau}}{\left(1 + C_2(x - \bar{x})^2 e^{\sigma_2\tau}\right)^2}$$

and

$$(s_2)_{xx}(x, \tau) = -\frac{2C_2 C_4 e^{(\sigma_2 - \sigma_4)\tau}}{\left(1 + C_2(x - \bar{x})^2 e^{\sigma_2\tau}\right)^2} + \frac{8C_2^2 C_4 (x - \bar{x})^2 e^{(2\sigma_2 - \sigma_4)\tau}}{\left(1 + C_2(x - \bar{x})^2 e^{\sigma_2\tau}\right)^3}.$$

Therefore the diffusion term in (30) becomes

$$r_1^{-2}e^{\tau/3}(s_2)_{xx} = -2\frac{C_2 C_4}{C_1^2}e^{(\sigma_2 - \sigma_4 - 2\sigma_1 + \frac{1}{3})\tau} + 8\frac{C_2^2 C_4}{C_1^2}\frac{(x - \bar{x})^2 e^{(2\sigma_2 - \sigma_4 - 2\sigma_1 + \frac{1}{3})\tau}}{1 + C_2(x - \bar{x})^2 e^{\sigma_2\tau}}. \tag{33}$$

Next we solve for C_4 and σ_4 to insure that (33) is equal to the residual in (30). This yields the following set of equations

$$2C_2 C_4 + 3C_1^2 C_3\sigma_3 = 0$$

$$\sigma_3 - \sigma_2 + \sigma_4 + 2\sigma_1 - \frac{1}{3} = 0$$

$$C_1^2 C_3\sigma_2 + 4C_2 C_4 = 0$$

$$\sigma_4 - \sigma_2 - \sigma_3 + 2\sigma_1 - \frac{1}{3} = 0.$$

Together with the relations (29) we find that

$$C_1^2 C_3\left(\frac{1}{3} + 2\sigma_3\right) + 4C_2 C_4 = 0$$

$$2C_2 C_4 + 3C_1^2 C_3\sigma_3 = 0 \tag{34}$$

$$\sigma_3 + \sigma_4 = \frac{2}{3}.$$

Combining the first two equations of (33) yields

$$\frac{1}{3} + 2\sigma_3 = 6\sigma_3.$$

Hence $\sigma_3 = 1/12$ and from the last equation in (33) we conclude that $\sigma_4 = 7/12$.

The above analysis gives the following approximation for the solution of (14) with initial data (26) and peak at $x = \bar{x}$:

$$
\begin{aligned}
r(x, \tau) &\approx C_1 \frac{e^{\tau/6}}{1 + C_2(x - \bar{x})^2 e^{\tau/2}} \\
s(x, \tau) &\approx \frac{1}{\sqrt{2C_1}} e^{-\tau/12} - \frac{C_1}{16C_2}\sqrt{2C_1} \frac{e^{-7\tau/12}}{1 + C_2(x - \bar{x})^2 e^{\tau/2}}.
\end{aligned}
\tag{35}
$$

We can continue this procedure to obtain a formal solution of (14) with initial data (26). Via (24), the new approximation for s leads to a new approximation of r. Next we choose $r_2(x, \tau)$ such that $\bar{r}(x, \tau) = r_1(x, \tau) + r_2(x, \tau)$ and $\bar{s}(x, \tau) = s_1(\tau) + s_2(x, \tau)$ is an exact solution of the equation for r. We compute the residual $R(\bar{r}, \bar{s})$ and find $s_3(x, \tau)$ by solving

$$\bar{r}(x, \tau)^{-2} e^{\tau/3} (s_3)_{xx}(x, \tau) = R(\bar{r}, \bar{s}).$$

In this way, we define a succession of functions that solve (14) with successively smaller residuals.

To measure the degree to which these approximate solutions solve the differential equation, we make a quantitative comparison of the computed numerical solution plotted in Fig. 16 with initial data (26) with the approximate solution given in (34).

We begin by comparing the approximate r and the numerical r. We plot the maximum of the numerical r versus τ in Fig. 17. After an initial transient period, r apparently grows at a steady exponential rate. Removing the transient in the data in Fig. 17 by restricting $\tau > 17.983$ as shown on the right, we compute a least squares line fit on the growth of the peak height at the location of the peak $\bar{x} \approx 0.68164$ to find

$$\hat{C}_1 \approx 0.785 \quad \text{and} \quad \hat{\sigma}_1 \approx 0.167 \approx \sigma_1 = 1/6,$$

where we use $\hat{q}$ to denote a measured value of a theoretical quantity q. The correlation of this line fit is $\rho^2 \approx 0.999999$.
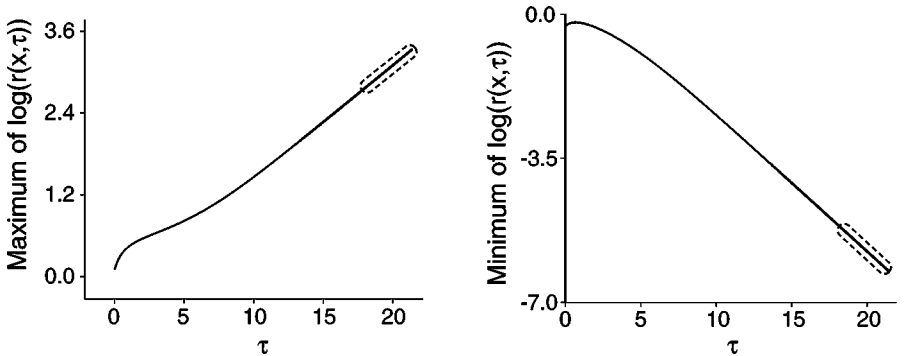

FIG. 17. Plots of the logarithm of the maximum and minimum heights of r versus τ for the computation shown in Fig. 16.
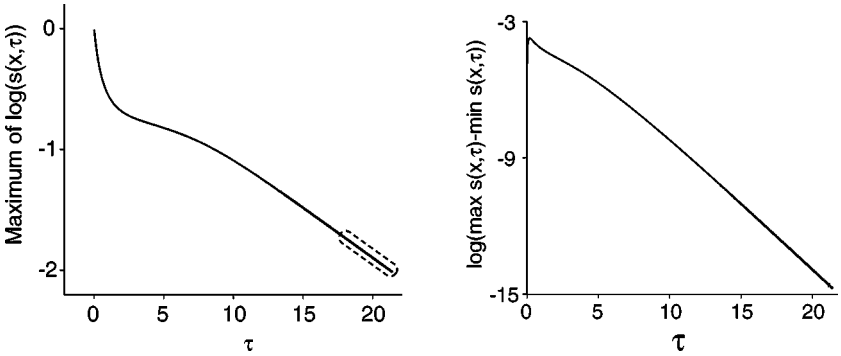
FIG. 18. Plots of the logarithm of the maximum height of s and the logarithm of the maximum of s subtract the minimum of s versus τ for the computation shown in Fig. 16.

As seen in Fig. 17, the minimum of r, which occurs at $x = 0$, appears to decrease exponentially after the initial transient. We scale out the growth in the peak height of r by computing

$$\frac{\hat{C}_1 e^{\hat{\sigma}_1 \tau}}{r(x, \tau)} - 1$$

and compute a least squares line fit to this data at $x = 0$. We find

$$\hat{C}_2 \approx 0.685 \quad \text{and} \quad \hat{\sigma}_2 \approx 0.500 \approx \sigma_2 = 1/2$$

with correlation $\rho^2 \approx 0.9999999999$.

The plot of s in Fig. 16 supports the Ansatz that s is nearly constant in x. In Fig. 18, we plot the maximum of s versus τ along with the difference of the maximum of s and the minimum of s. We use least squares to fit a line to the data shown in Fig. 18 for $\tau > 17.983$ to find

$$\hat{C}_3 \approx 0.792 \quad \text{and} \quad \hat{\sigma}_3 \approx 0.083 \approx \sigma_3 = 1/12$$

with correlation $\rho^2 \approx 0.999999$ while the difference in the maximum and minimum value of s decreases exponentially at an approximate rate of 0.89. In every case, the computed values of the parameters are very close to the values of the parameters in the approximate solution (34).

We are unable to compute reliable numerical values for the parameters in the higher order terms in the model because of subtractive cancellation errors that arise because s tends to zero everywhere at an exponential rate. A visual comparison of the computed and predicted values of s is compelling evidence, however. We plot the final profile of s versus x in Fig. 19 along with the predicted profile computed from (34) using values for C_1, C_2, and τ computed in the analysis of r above. Since the parameter values are only accurate to within two places, these plots suggest a remarkably close agreement. In particular, note that the profiles of the computed and predicted functions are very similar.

However, the magnitude of the approximate and computed s agree to only two decimal digits. The reason is that the computed solution begins with arbitrary data that is not close
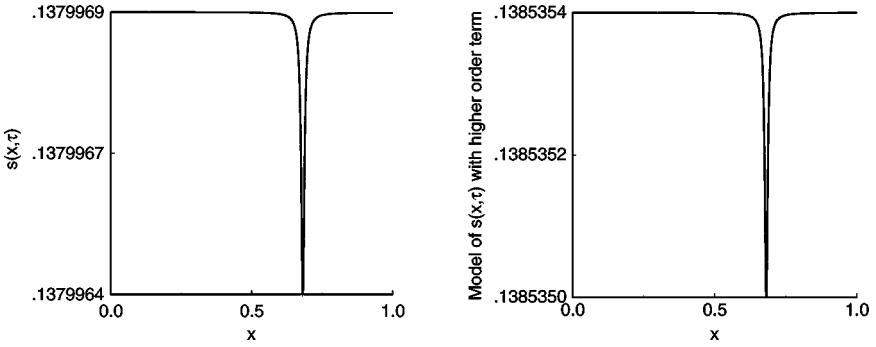
FIG. 19. Plot of the numerical solution for s and the predicted value from (34) at $\tau \approx 21$.

to a blow-up profile. In particular, the values of C_1, C_2, C_3, $\bar{x}$, and γ do not satisfy the equations relating these parameters. One serious consequence of this discrepancy is that $\bar{x}$ moves from 0.7 in the data to 0.68164 in the final solution, which violates the simplifying assumption (29).

To obtain more natural initial data, we compute a new solution of (14) starting with data (26) using values $C_1 = \hat{C}_1$, $C_2 = \hat{C}_2$, $C_3 = \hat{C}_3$, and $\bar{x} = 0.68164$ obtained from the first numerical solution and then repeat the least squares model fit to compute new values of the parameters. This second solution has a peak at $\bar{x} = 0.67480$, which means that the change in $\bar{x}$ from the initial value to the final value in the two solutions decreases from 0.01836 to 0.00694. Repeating this process several times, we find rapid convergence to initial data for which $\bar{x}$ does not move from the initial value. We list the parameter values computed from four iterations in Table I.

There is a practical difficulty with this iterative process to produce "good" initial data. Namely, the values of $\hat{C}_2$ decrease for each iteration. This means that each subsequent initial data r_0 becomes significantly broader. Consequently, the solutions take increasingly large times to form a peak that is large enough to compute the parameter values accurately. In fact, the peak height of the solution in the third iteration is less than 0.8. For this reason, the remarkable accuracy in the parameter values $\hat{\sigma}_1$, $\hat{\sigma}_2$, and $\hat{\sigma}_3$ obtained for the first iteration degrades in the following iterations.

To quantify the relation between the approximate s and the computed s from the four iterations, we plot the ratios of the approximate $s(x, \tau)$ to the computed $s(x, \tau)$ versus x in Figs. 20 and 21.

TABLE I

The Parameter Values in the Approximate Solutions Computed from the Numerical Solutions Using Least Squares Line Fits for Four Iterations of Initial Data

Iteration	Initial $\bar{x}$	Final $\bar{x}$	$\hat{\sigma}_1$	$\hat{C}_1$	$\hat{\sigma}_2$	$\hat{C}_2$	$\hat{\sigma}_3$	$\hat{C}_3$
0	0.700	0.68164	0.167	0.785	0.500	0.685	0.083	0.792
1	0.68164	0.67480	0.1666	0.349	0.5000	0.302	0.083	1.20
2	0.67480	0.67285	0.166	0.113	0.500	0.0969	0.083	2.09
3	0.67285	0.67285	0.166	0.0223	0.50	0.0190	0.082	4.68

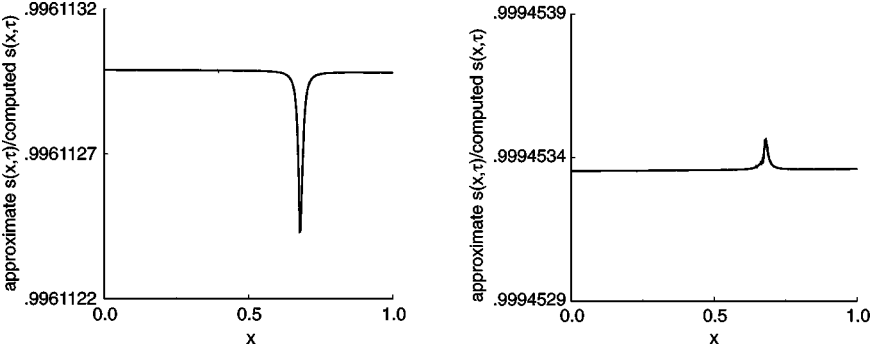*Note.* The correlations of the various fits were greater than 0.999999.

FIG. 20. Plots of the ratio of both of the approximate solution s to the computed solution s versus x at $\tau \approx 21$ for iteration 0 (left) and 1 (right).

It turns out that if $\bar{x} = 0.5$ in the initial data (26), then $\bar{x} = 0.5$ for all τ. Thus we avoid the problem of $\bar{x}$ moving during an initial transient for that special class of data. We show the computed solution starting with $C_1 = 1.108422867$, $C_2 = 1$, $C_3 = 1$, and $\bar{x} = 0.5$ in Fig. 22. We give the computed parameter values in Table II. The ratio of the approximate s to the computed s values, given in Table II, is very close to 1.

To summarize, experimentally we find that generic numeric solutions starting from data (26) converge to the approximate solution after an initial transient period while solutions that satisfy the assumptions and Ansatz underlying the analysis agree very well for all time.

The approximate solution (34) which we have derived for the special initial data (26) suggests the following model of the behavior of r near the peak for more general initial data

$$\tilde{r}(x, \tau) = \frac{A(x)e^{\sigma_1 \tau}}{1 + B(x)e^{\sigma_2 \tau}}, \tag{36}$$

where $A(x) > 0$, $B(\bar{x}) = 0$, and $\sigma_2 > \sigma_1$. The model function allows exponential growth with rate σ_1 at $\bar{x}$ and exponential decay with rate $\sigma_2 - \sigma_1$ away from $\bar{x}$.

The initial data used for the computations shown in Figs. 7, 8, and 10 are

$$r_0(x)^2 = \begin{cases} 1 + 1880(x - 0.64)^2(x - 0.84)^2, & 0.64 < x < 0.84 \\ 1, & \text{otherwise} \end{cases} \tag{37}$$
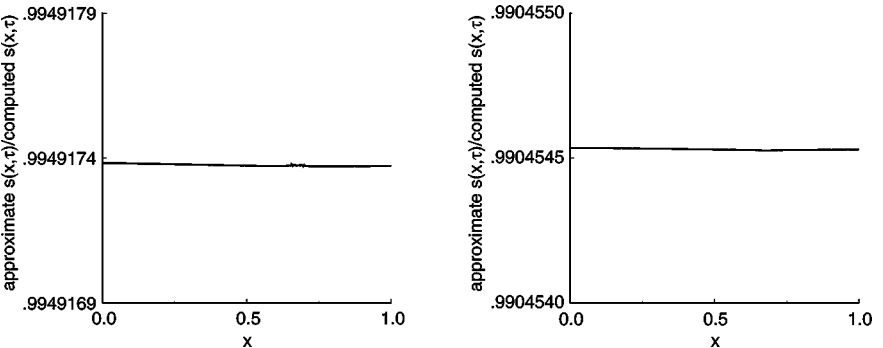
$$s_0(x) = 1.$$

FIG. 21. Plots of the ratio of both of the approximate solution s to the computed solution s versus x at $\tau \approx 21$ for iteration 2 (left) and 3 (right).
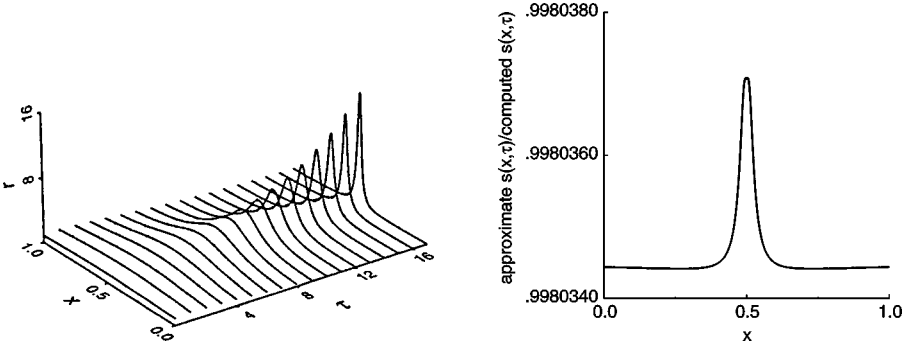
FIG. 22. Plots of the evolution of r versus τ starting with the initial data (26) with $\bar{x} = 0.5$ and the ratio of the approximate s to the computed s.

This gives a smooth "bump" in r_0 centered at 0.74 of width 0.2 and amplitude approximately 0.1. To analyze whether the suggested model for r does capture the behavior of r near the peak, we first plot the maximum of r and s versus τ in Fig. 23 for the computation shown in Fig. 10. After a long initial transient period, r apparently grows at a steady exponential rate while s tends to zero at a steady exponential rate.

Removing the transient in the data in Fig. 23 by restricting $\tau > 13.2$, we compute a least squares line fit on the growth of the peak height at $\bar{x} = 0.8$ to find

$$A(\bar{x}) \approx 3.34 \quad \text{and} \quad \hat{\sigma}_1 \approx 0.17 \approx \frac{1}{6}.$$

The correlation of this line fit is $\rho^2 \approx 0.99999$.

The minimum of r appears to decrease exponentially after the initial transient. We plot the minimum of r in Fig. 24. We scale out the growth in the peak height of r by computing

$$\frac{A(\bar{x})e^{\hat{\sigma}_1 \tau}}{r(x, \tau)} - 1$$

and compute a least squares line fit to this data at $x = 0.79980$, where the minimum of $r(x, \cdot)$ is obtained. We find

$$\hat{\sigma}_2 \approx 0.50$$

with correlation $\rho^2 \approx 0.9999999999$. Hence, in the model (36) for r, we take, as for the special initial data,

$$\sigma_1 = 1/6 \quad \text{and} \quad \sigma_2 = 1/2.$$

TABLE II
The Parameter Values in the Approximate Solution Computed from the Numerical Solution Using Least Squares Line Fits

Initial $\bar{x}$	Final $\bar{x}$	$\hat{\sigma}_1$	$\hat{C}_1$	$\hat{\sigma}_2$	$\hat{C}_2$	$\hat{\sigma}_3$	$\hat{C}_3$
0.50000	0.5000	0.166	0.836	0.500	0.711	0.083	0.769

Note. The correlations of the various fits were greater than 0.999999.
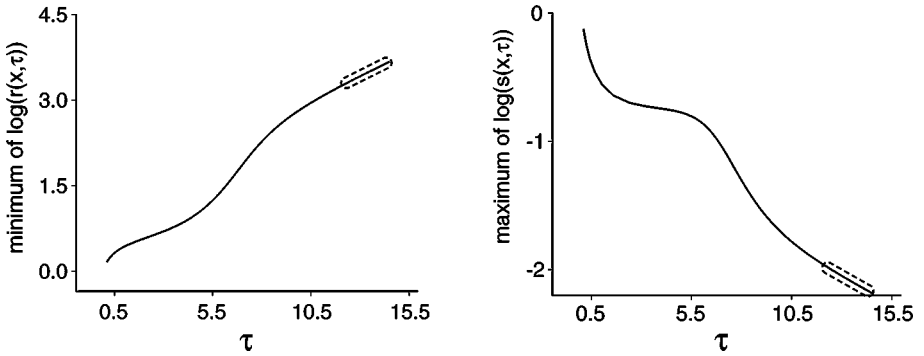
FIG. 23. Plots of the logarithm of the maximum height of r and s versus τ for the computation shown in Fig. 10.

Substituting $\tilde{r}$ into the ordinary equation defining r in (14) along with $\alpha = 2$, we can solve for the model of s,

$$\tilde{s}(x, \tau) = \frac{1}{\sqrt{2}\sqrt{A(x)}e^{\sigma_3 \tau}} \tag{38}$$

with

$$\sigma_3 = 1/12.$$

We verify that s is close to $\tilde{s}$ numerically. Using the values of the maximum of s shown in Fig. 23, we determine the exponential rate of decrease of s as $\hat{\sigma}_3 \approx 0.088$ with correlation $\rho^2 = 0.99997$. Recall that the predicted rate is $\sigma_3 = 1/12 \approx 0.083$. From (38), we predict the value of $C_3 = 1/\sqrt{2C_1} \approx 0.39$ while the computed value is $\hat{C}_3 \approx 0.40$. In addition, computing a least squares line fit on the data for s shown in Fig. 24, we find that after the transient the difference in the maximum and minimum values of s decreases exponentially with rate 0.83 with correlation $\rho^2 = 0.99997$. Thus s approaches a constant profile in x much more rapidly than it decreases to zero.

The functions $\tilde{r}$ and $\tilde{s}$ are not solutions to (14) and substituting these functions into (14) therefore leads to a nonzero residual. If we require that this residual tend to 0 as $\tau \to \infty$,

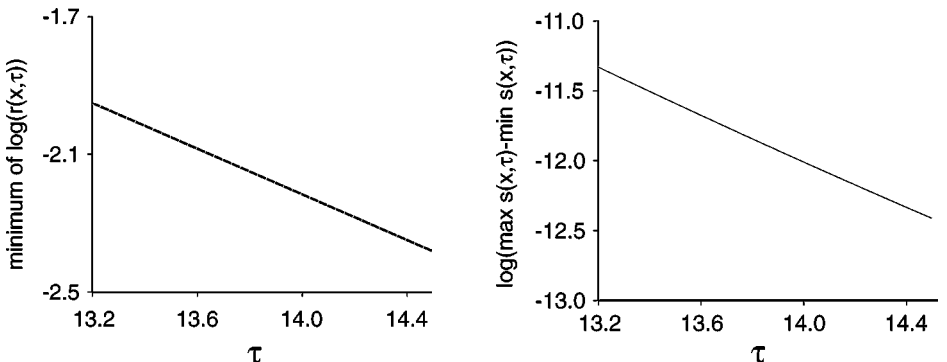**FIG. 24.** On the left, we plot the logarithm of the minimum height of r versus τ for the computation shown in Fig. 10. The minimum of $r(x, \tau)$ occurs for $x = 0$. On the right, we plot the logarithm of the difference between the maximum and minimum values of s versus τ.
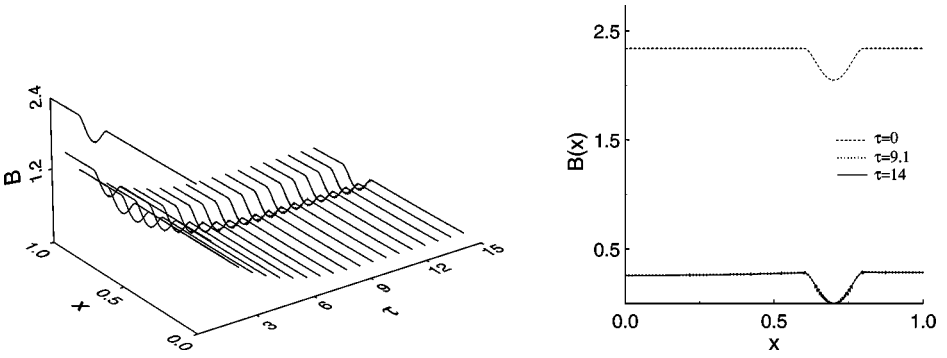
FIG. 25. On the left, we plot the evolution of $B(x)$ for the computation shown in Fig. 10. On the right, we plot $B(x)$ versus x for $\tau \approx 0, 9.1$, and 14. The plots for $\tau \approx 9.1$ and $\tau \approx 14$ are indistinguishable.

we obtain a differential equation for the coefficient A:

$$-3(A'(x))^2 + 2A''(x)A(x) = 0, \quad 0 < x < 1. \tag{39}$$

Separation of variables yields two solutions of this equation

$$A(x) = C_1 \quad \text{and} \quad A(x) = \frac{C_1}{(x + C_1)^2}$$

for some constant C_1. The second choice for A does not correspond with the observed behavior of r and therefore, $A(x)$ has to be constant.

Specifying that the residual tend to zero as τ tends to infinity does not put any condition on $B(x)$. Rather $B(x)$ is determined by the initial data through the limiting behavior of the solutions. We can compute an approximate representation of B using the formula

$$B(x) = \frac{C_1 \, e^{-\tau/3} - r(x, \tau)e^{-\tau/2}}{r(x, \tau)}. \tag{40}$$

We plot the computed $B(x)$ in Fig. 25. The plots of B become indistinguishable for $\tau > 9$, which supports the contention that the solution is converging to the model function at $\tau \to \infty$.

To end this section, we plot in Fig. 26 the numerical solutions v and θ corresponding to the numerical solution r and s shown in Fig. 16. In terms of the physical variables, the
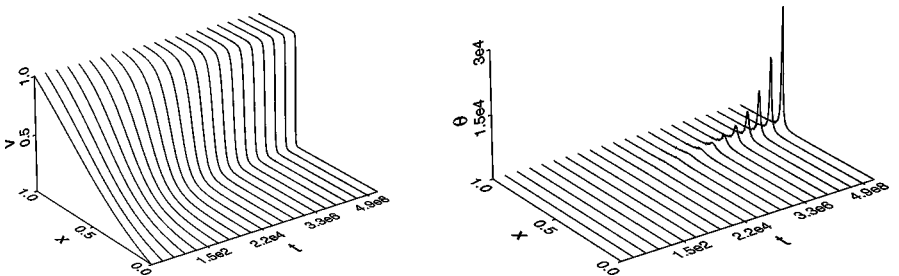

FIG. 26. Plots of the evolution of v and θ versus τ starting with the initial data (26).

approximate solution (34) becomes

$$\tilde{\sigma}(x,t) = \frac{1}{\sqrt{2C_1}}(t+1)^{-3/4} \quad \text{and} \quad \tilde{\theta}(x,t) = \frac{C_1(t+1)^{1/2}}{1 + C_2(x-\bar{x})^2(t+1)^{1/2}}.$$

Finally, we compute

$$\tilde{v}_x(x,t) = \frac{C_1^{3/2}(t+1)^{1/4}}{2^{1/2}\left(1 + C_2(x-\bar{x})^2(t+1)^{1/2}\right)^2}.$$

5. THE STABILITY OF THE MODEL FOR SHEAR LAYERS

In this section, we study the effect of the choice of the initial data r_0 and s_0 on the convergence of r and s to the model functions $\tilde{r}$ and $\tilde{s}$. We begin by presenting examples of solutions corresponding to various sizes of perturbation from the constant in r_0. Then we show a solution in which a high frequency, small amplitude perturbation is added to r_0. Following that, we consider the effect of altering the center of the perturbation $\bar{x}$ in r_0. Finally, we present examples in which s_0 is perturbed slightly in various ways. The numerical results in this section strongly suggest that the model functions are stable in the sense that solutions corresponding to a wide range of smooth data r_0 and s_0 converge to the model functions as $\tau \to \infty$.

In the following computations, we take the initial data used for the solutions plotted in Figs. 7, 8, and 10 as the base for comparison. We repeated these computations with the special solution with data (26) as well as other shapes of initial perturbations in r_0. In all cases, we obtain results comparable to those we report here.

5.1. *Varying the Size of the Initial Bump in r_0*

The initial data used for the computations shown in Figs. 7, 8, and 10 are

$$r_0(x)^2 = \begin{cases} 1 + \frac{16\mathcal{A}}{\mathcal{W}^4}(x - \bar{x} - \mathcal{W}/2)^2(x - \bar{x} + \mathcal{W}/2)^2, & \bar{x} - \mathcal{W}/2 < x < \bar{x} + \mathcal{W}/2 \\ 1, & \text{otherwise} \end{cases}$$

$$s_0(x) = 1$$

(41)

with $\bar{x} = 0.74$, $\mathcal{A} = 0.2$, and $\mathcal{W} = 0.2$. This gives a smooth "bump" in r_0 centered at $\bar{x}$ of width $\mathcal{W}$ and amplitude approximately $\frac{1}{2}\mathcal{A}$.

In this section, we present solutions corresponding to data of the form (41) for special choices of $\mathcal{A}$ and $\mathcal{W}$. The various choices are listed in Table III and the corresponding initial data r_0 are shown in Fig. 27.

Altering the data for r affects the length of the transient period. We plot the maximum peak height on a log scale of r and s in Fig. 28. Nonetheless, the curves for the solutions become roughly parallel after some initial transient period.

In Fig. 29, we plot the profiles of $r(x, \tau)$ versus x at τ when the maximum height of r is approximately 40. It is evident that the profiles of r have the same shape in the region of the peak, and this shape is dictated by the form of the model. We plot the corresponding functions $B(x)$ in the models in Fig. 29 as well. These functions also have the same basic shape.

In Table IV, we list the parameter values in the model functions $\tilde{r}$ and $\tilde{s}$ computed from the numerical solutions r and s using the least squares fits described in Section 4. All of the

TABLE III

The Parameter Values for the First Set of Initial Data

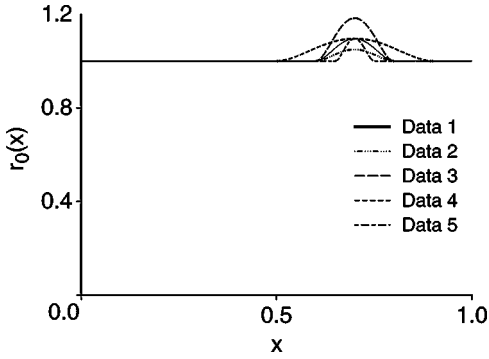| Data number	$\mathcal{W}$	$\mathcal{A}$	$\bar{x}$
1	0.2	0.2	0.7
2	0.2	0.1	0.7
3	0.2	0.4	0.7
4	0.4	0.2	0.7
5	0.1	0.2	0.7

FIG. 27. The plots of $r_0(x)$ corresponding to the parameter values given in Table 3.
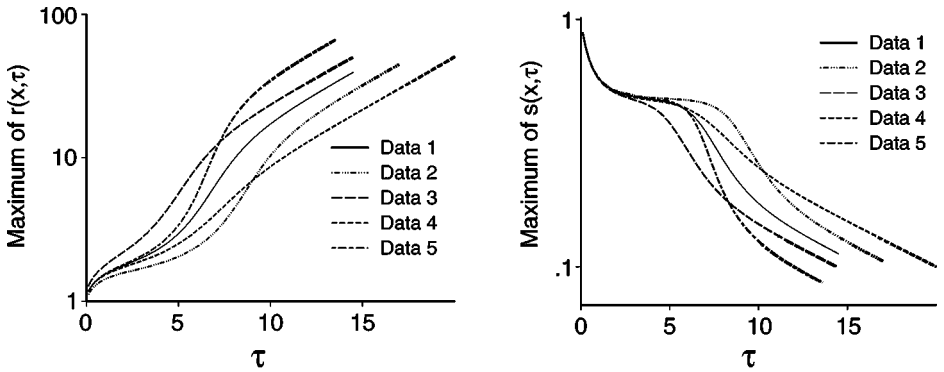
FIG. 28. Plots of the maximum heights of r and s versus τ on a log scale for the solutions with data given in Table 3.
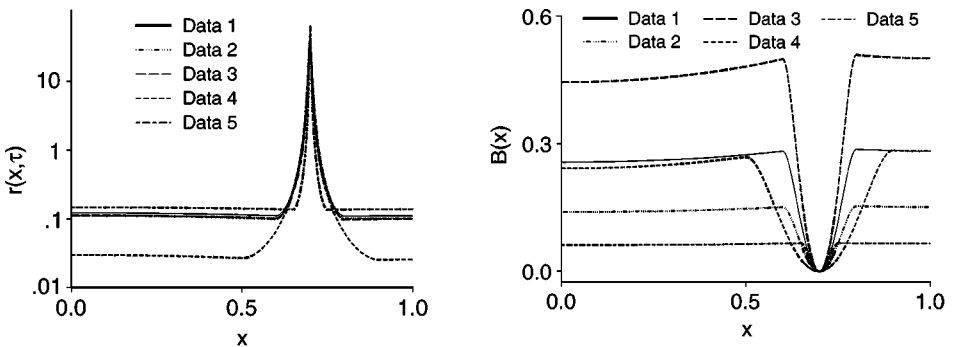

FIG. 29. Plots of $r(x, \tau)$ versus x at τ when the height of $r \approx 40$ along with plots of the functions $B(x)$.

<div align="center">

TABLE IV

**The Parameter Values in the Model Functions $\tilde{r}$ and $\tilde{s}$ Computed
from the Numerical Solutions Using Least Squares Line Fits**

</div>

Data	σ_1	C_1	σ_2	σ_3	C_3	Predicted C_3
1	0.167	3.5	0.500	0.086	0.39	0.38
2	0.17	2.5	0.50	0.087	0.46	0.45
3	0.17	4.6	0.50	0.085	0.34	0.33
4	0.17	1.6	0.51	0.083	0.53	0.56
5	0.17	6.8	0.50	0.089	0.29	0.27

Note. The correlations of the various fits were greater than 0.999999.

numbers agree with the values predicted by the model to one place and most agree to
two places. Accurate values for Data 5, which is the narrower bump, are more difficult to
compute because the peak in r is narrower in the beginning. We computed the solutions for
Data 5 beginning with twice as many initial space mesh points as for the other computations.

We computed a variety of different bump sizes and also used other shapes and obtained
similar results in every case. The numerical evidence supports the conjecture that various
smooth perturbations in the initial constant profile lead to solutions that converge to their
respective model functions.

5.2. *Introducing a Small Amplitude, High Frequency Oscillation in r_0*

We add a perturbation of the form $\epsilon(x)$,

$$\epsilon(x) = 0.05 \times \cos(11\pi x)$$

to the initial data (41) with $\bar{x} = 0.74$, $\mathcal{A} = 0.2$, and $\mathcal{W} = 0.2$ to get Data 6. We plot the
initial data and the evolution of r in Fig. 30.

From the plot, it is possible to see that the small amplitude perturbations persist in the
solution as τ increases, but they become increasingly insignificant in height relative to the
forming peak. In Fig. 31, we plot the profiles of $r(x, \tau)$ and the corresponding $B(x)$ versus
x at $\tau \approx 14$. The formation of the peak is the same in shape, width, etc., but interestingly,
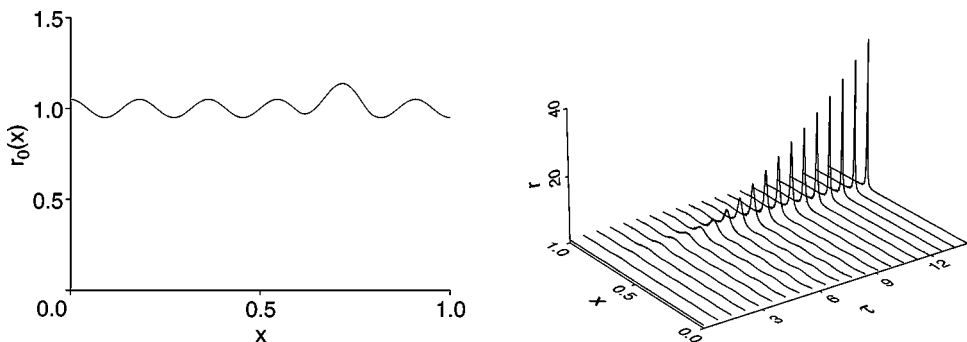

FIG. 30. Plots of the initial Data 6 and the subsequent evolution of r versus τ.
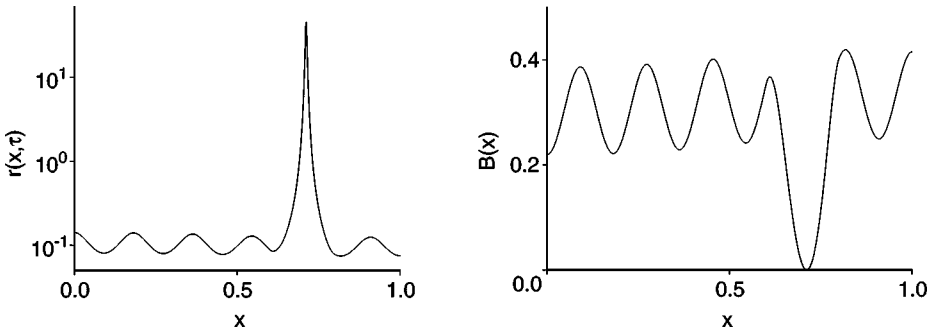
FIG. 31. Plots of $r(x, \tau)$ and $B(x)$ versus x at $\tau \approx 14$.

the location of the peak moves from 0.7 in the initial data to 0.71 in the final solution. In Fig. 32, we plot the profile of $s(x, \tau)$ versus x at $\tau \approx 14$. The legacy from the initial perturbation is apparent in $B(x)$ but as can be expected, the oscillations in s are damped out by the large diffusion that exists outside the immediate neighborhood of the peak in r.

Altering the data for r again affects the length of the transient period. We plot the maximum peak height on a log scale of r and s in Fig. 33. Nonetheless, the curves for the solutions corresponding to the unperturbed and perturbed solutions become roughly parallel after some initial transient period.

In Table V, we list the parameter values in the model functions $\tilde{r}$ and $\tilde{s}$ computed from the numerical solutions r and s using the least squares fits described in Section 4 for the unperturbed and perturbed solutions. Again we get very good agreement between the parameters for the two computations.

We computed similar examples using a variety of regular and irregular small amplitude, high frequency perturbations in r_0 and obtained similar results. The numerical evidence suggests that the formation of the shear layer dominates the dynamical behavior of solutions of (14) and that a wide class of solutions converge to the model functions.

5.3. Varying the Location of the Initial Bump in r_0

In this section, we present numerical results for solutions that begin with the "bump" in r_0 centered at different points $\bar{x}$. We compare the solution corresponding to initial data (41)
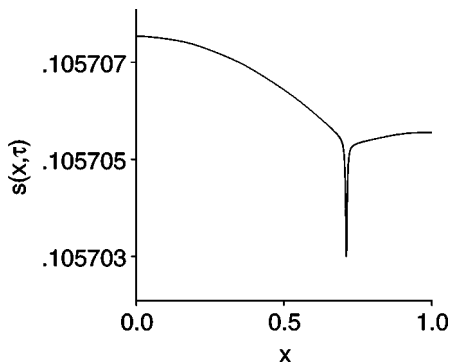

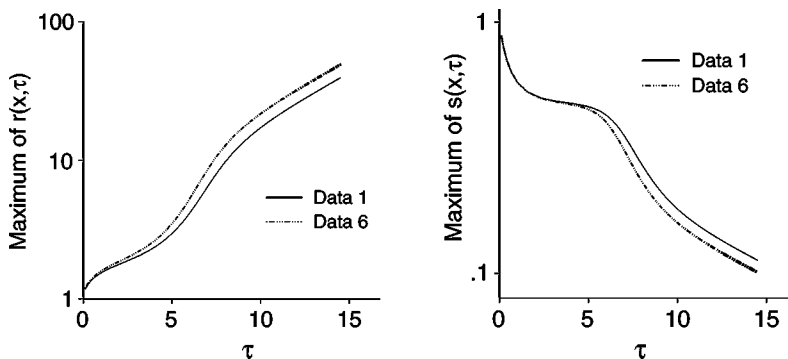**FIG. 32.** Plot of $s(x, \tau)$ versus x at $\tau \approx 14$.

FIG. 33. Plots of the maximum heights of r and s versus τ for Data 1 and 6 on a log scale.

with $\mathcal{A} = 0.2$, $\mathcal{W} = 0.2$, and $\bar{x} = 0.6$ (Data 7) and $\bar{x} = 0.8$ (Data 8) to the original Data 1 with $\bar{x} = 0.7$.

Moving the location of the bump affects little. This is evident in the plots of the maximum peak height on a log scale of r and s in Fig. 34. In Table VI, we list the parameter values in the model functions $\tilde{r}$ and $\tilde{s}$ computed from the numerical solutions r and s using the least squares fits described in Section 4 for three different solutions.

We repeated these computations with the initial perturbation located at a variety of positions through $[0, 1]$ and obtained similar results for all computations. The numerical evidence suggests that moving the location of the perturbation has little effect on the convergence of solutions to the model functions.

5.4. Introducing Perturbations into the Initial Profile of s_0

In contrast to previous sections, we now consider the effect of an initial perturbation in the value of s_0. To construct Data 9, we add a small amplitude, high frequency perturbation $\epsilon(x)$,

$$\epsilon(x) = 0.1 \times \cos(11\pi x)$$

to s_0 in (41). It turns out that adding perturbations to s_0 that are relatively small compared to the perturbations to r_0 has little effect on the solutions.

In Fig. 35, we plot the profiles of $r(x, \tau)$ and the corresponding $B(x)$ versus x at $\tau \approx 14$. In Fig. 36, we plot the profile of $s(x, \tau)$ versus x at $\tau \approx 14$. The close agreement in these profiles show that the perturbations in s_0 have little effect in the end.

TABLE V

The Parameter Values in the Model Functions $\tilde{r}$ and $\tilde{s}$ Computed from the Numerical Solutions Using Least Squares Line Fits

Data	σ_1	C_1	σ_2	σ_3	C_3	Predicted C_3
1	0.167	3.5	0.500	0.086	0.39	0.38
6	0.17	4.1	0.51	0.087	0.36	0.35

Note. The correlations of the various fits were greater than 0.999999.

TABLE VI

The Parameter Values in the Model Functions $\tilde{r}$ and $\tilde{s}$ Computed from the Numerical Solutions Using Least Squares Line Fits

Data	σ_1	C_1	σ_2	σ_3	C_3	Predicted C_3
1	0.167	3.5	0.500	0.086	0.39	0.38
7	0.17	3.3	0.51	0.087	0.40	0.39
8	0.17	3.2	0.51	0.087	0.40	0.40

Note. The correlations of the various fits were greater than 0.999999.
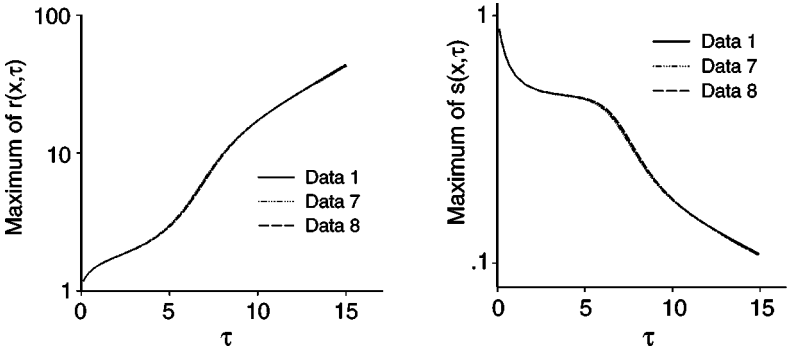
FIG. 34. Plots of the maximum heights of r and s versus τ on a log scale.
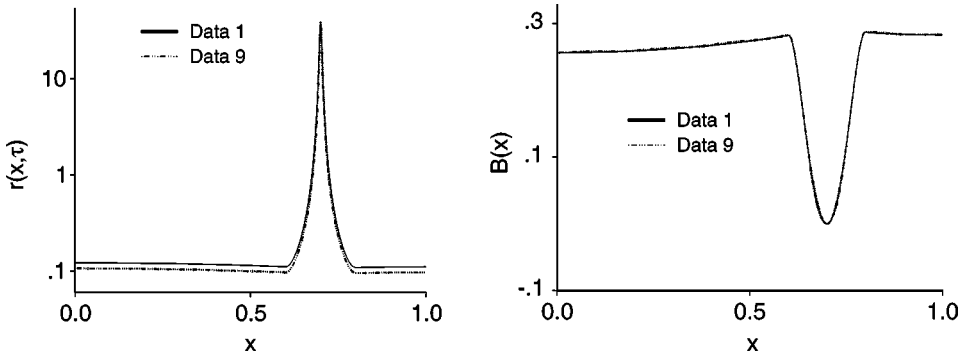

FIG. 35. Plots of $r(x, \tau)$ and $B(x)$ versus x at $\tau \approx 14$ for Data 1 and 9.
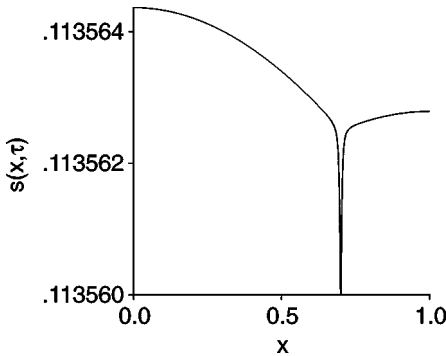

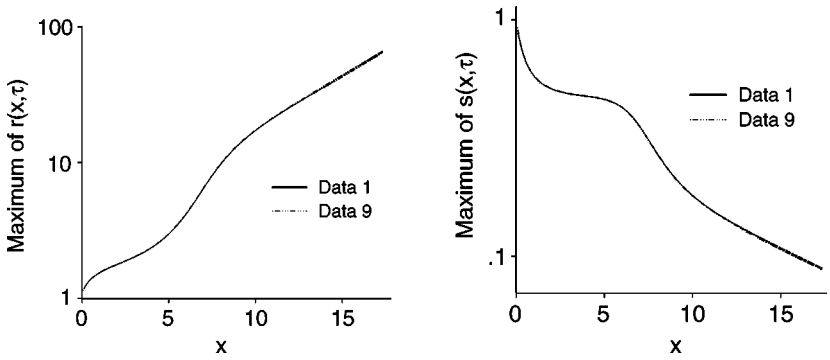**FIG. 36.** Plot of $s(x, \tau)$ versus x at $\tau \approx 14$ for Data 1 and 9.

FIG. 37.   Plots of the maximum heights of r and s versus τ for Data 1 and 9 on a log scale.

This is reflected in the length of the transient period, which is hardly altered. We plot the maximum peak height on a log scale of r and s in Fig. 37. Finally, we list the parameter values in the model functions computed from the solutions in Table VII.

We computed several examples of solutions that begin with the same perturbation in r_0 and various small amplitude perturbations in s_0 and obtained similar results in every case. The numerical evidence suggests that initial perturbations in s_0 that are small compared to the initial perturbations in r_0 have little effect on the solutions.

We finish this section by considering the solution corresponding to an initial perturbation in s_0 while r_0 is constant. More precisely, the initial Data 10 is

$$s_0(x) = \begin{cases} 1 + \frac{16\mathcal{A}}{\mathcal{W}^4}(x - \bar{x} - \mathcal{W}/2)^2(x - \bar{x} + \mathcal{W}/2)^2, & \bar{x} - \mathcal{W}/2 < x < \bar{x} + \mathcal{W}/2 \\ 1, & \text{otherwise} \end{cases}$$

$$r_0(x) = 1,$$
(42)

with $\bar{x} = 0.74$, $\mathcal{A} = 0.2$, and $\mathcal{W} = 0.2$. This gives a smooth "bump" in s_0 centered at $\bar{x}$ of width $\mathcal{W}$ and amplitude $\mathcal{A}$. We plot the evolution of r and s in Fig. 38.

While the initial perturbation to s_0 is damped out, it is still sufficient to cause a peak to grow in r, albeit after a much longer transient period than we have seen so far. In Fig. 39, we plot the profiles of $r(x, \tau)$ and the corresponding $B(x)$ versus x at $\tau \approx 29$. The peak is centered at 0.71 although the initial bump in s_0 is centered at 0.7. In Fig. 40, we plot the profile of $s(x, \tau)$ versus x at $\tau \approx 29$. Both the late profile of s and B are altered a little bit from the corresponding plots for Data 1.

These data clearly lead to a longer transient period. We plot the maximum peak height on a log scale of r and s in Fig. 41. Nonetheless, the curves for Data 1 and Data 10 become roughly parallel after some initial transient period.

TABLE VII
The Parameter Values in the Model Functions $\tilde{r}$ and $\tilde{s}$ Computed
from the Numerical Solutions Using Least Squares Line Fits

Data	σ_1	C_1	σ_2	σ_3	C_3	Predicted C_3
1	0.167	3.5	0.500	0.086	0.39	0.38
9	0.17	3.2	0.51	0.087	0.40	0.39

Note. The correlations of the various fits were greater than 0.999999.
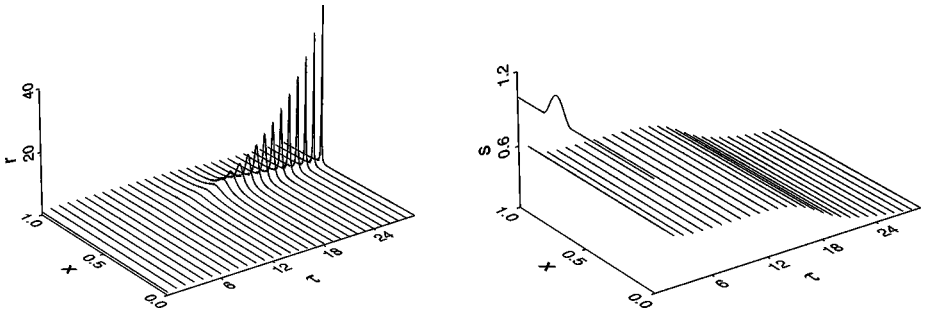
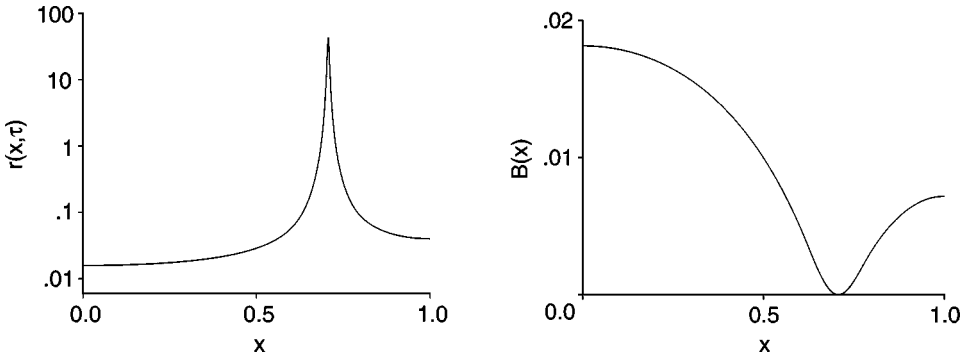**FIG. 38.** Plots of the evolution of r and s versus τ for Data 10.

FIG. 39. Plots of $r(x, \tau)$ and $B(x)$ versus x at $\tau \approx 29$.
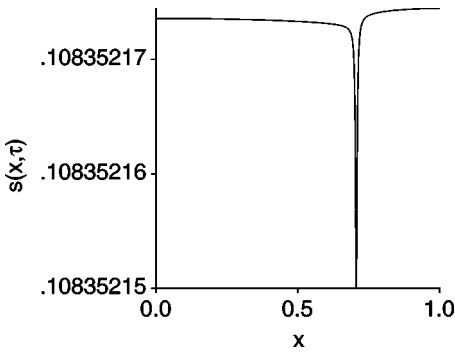

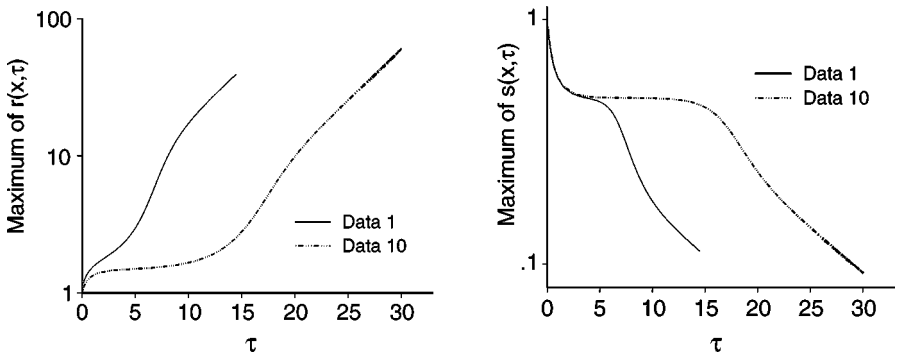**FIG. 40.** Plot of $s(x, \tau)$ versus x at $\tau \approx 29$.

FIG. 41. Plots of the maximum heights of r and s versus τ for Data 1 and 10 on a log scale.

TABLE VIII

The Parameter Values in the Model Functions $\tilde{r}$ and $\tilde{s}$ Computed from the Numerical Solutions Using Least Squares Line Fits

Data	σ_1	C_1	σ_2	σ_3	C_3	Predicted C_3
1	0.167	3.5	0.500	0.086	0.39	0.38
10	0.17	0.32	0.51	0.084	1.1	1.3

Note. The correlations of the various fits were greater than 0.999999.

In Table VIII, we list the parameter values in the model functions $\tilde{r}$ and $\tilde{s}$ computed from the numerical solutions r and s using the least squares fits described in Section 4 for the unperturbed and perturbed solutions. Again we get very good agreement between the parameters for the two computations.

These numerical results give further evidence that the formation of the shear layer dominates the dynamical behavior of solutions to (14) and that a wide class of solutions converge to the model functions. In the next section we give more evidence of this fact by varying the choice of initial data even further.

6. VARIATIONS IN THE MODEL EQUATIONS AND DATA

To this point, we have restricted the investigation to considering solutions that begin with data that are close to one of two functions, namely the "smooth bump" and the special solution, and to $\alpha = 2$. In this section, we widen the consideration to more exotic choices of data and also to variations in α and even in the differential equations themselves. In some cases, we get results that are closely connected to the results obtained in the previous sections. In other cases, we get new and interesting behavior that point to the complicated nonlinear nature of (14).

6.1. Multiple Peaks

We previously considered the effect of adding a small amplitude, high frequency perturbation $\epsilon(x)$,

$$\epsilon(x) = a \times \cos(11\pi x) \tag{43}$$

to the bump data (41) and saw that it had little effect on the formation of the largest peak in the solution. It is natural to consider the effect of adding such perturbations to initial constant values for r and s. In Fig. 42, we plot the evolution of r and v versus τ and t for the solution corresponding to Data 11 obtained by adding (43) with $a = 0.02$ to the initial $r_0 = 1$. In Fig. 43, we plot the evolution of r and v versus τ and t for the solution corresponding to Data 12 obtained by adding (43) with $a = 0.1$ to the initial $s_0 = 1$. We see the solutions develop several peaks of the same shape as those analyzed previously. The solution corresponding to the initial perturbation in s_0 has a much longer transient period.

Solutions corresponding to very broad initial data can also form more than one peak. We form initial data by altering (26) to get Data 13,

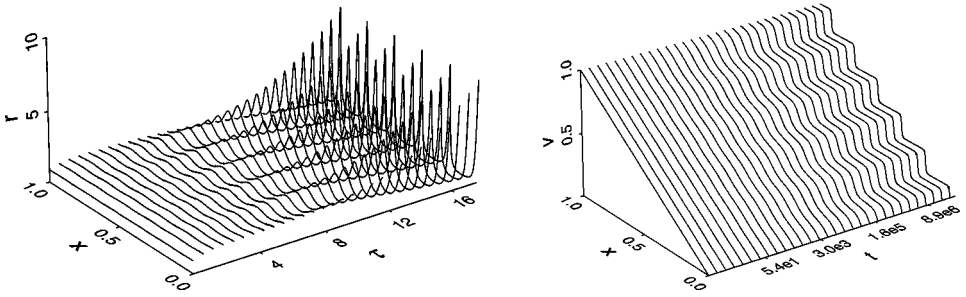$$r_0(x) = \frac{1.01223170451293}{1 + (x - 0.5)^4}$$

FIG. 42. Plots of the evolution of r and v versus τ and t for Data 11.

and $s_0 = 1$ so that both r_0 and s_0 are symmetric about $x = 0.5$. We plot the evolution of r and v versus τ and t in Fig. 44. Interestingly, one very broad peak initially develops but the center "collapses" and two peaks are left to grow. Both peaks, centered at 0.40322 and 0.59678, respectively, appear to be growing at the same rate and with the same profile. We compare the parameter values in the model computed by least squares for the solutions corresponding to Data 0 and Data 13 in Table IX. For Data 13, the model is fitted to the left-hand peak.

6.2. Reversing the Initial Perturbation

It is natural to consider the solution corresponding to (41) with $\mathcal{A} = -0.2$, $\mathcal{W} = 0.2$, and $\bar{x} = 0.7$, in other words with an initial "dip" rather than a "bump". We label this as Data 14. The resulting solution is very interesting. We plot the evolution of the solution in Fig. 45 and the final s and r profiles in Fig. 46. The solution appears to form two extremely sharp "spikes" at the positions where the initial data have discontinuities in the second derivative. The spikes have profiles similar to those of other solutions on one side, but on the other side they appear much steeper, even suggesting that the solution might lose differentiability at the tips. This loss of regularity is also reflected in the profile of s. Interestingly, one spike appears to dominate the other. We study the "competition" between spikes in more detail below.

6.3. Competition Between Spikes

We have seen several examples now of initial data leading to solutions with several spikes. In this section, we consider the interaction of two spikes in one solution. It appears that
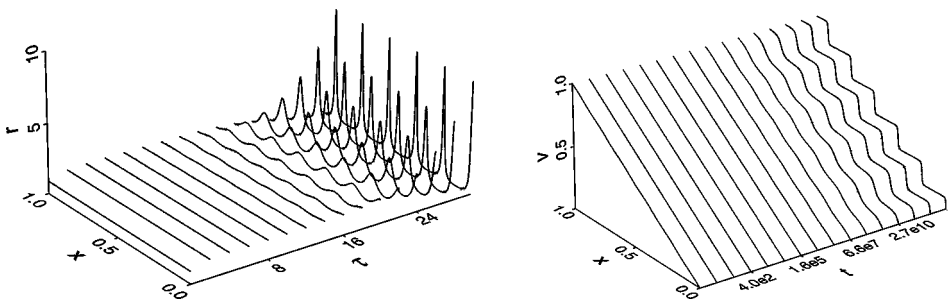

FIG. 43. Plots of the evolution of r and v versus τ and t for Data 12.

TABLE IX

**The Parameter Values in the Model Functions $\tilde{r}$ and $\tilde{s}$ Computed
from the Numerical Solutions Using Least Squares Line Fits**

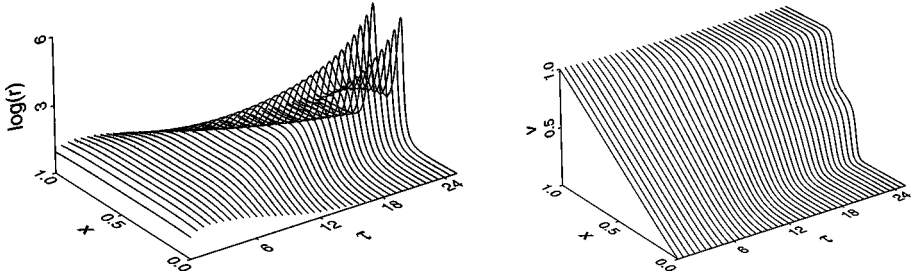| Data	σ_1	C_1	σ_2	σ_3	C_3	Predicted C_3
0	0.167	0.785	0.500	0.0831	0.792	0.798
13	0.16	0.10	0.49	0.062	1.4	1.3

Note. The correlations of the various fits were greater than 0.999999.

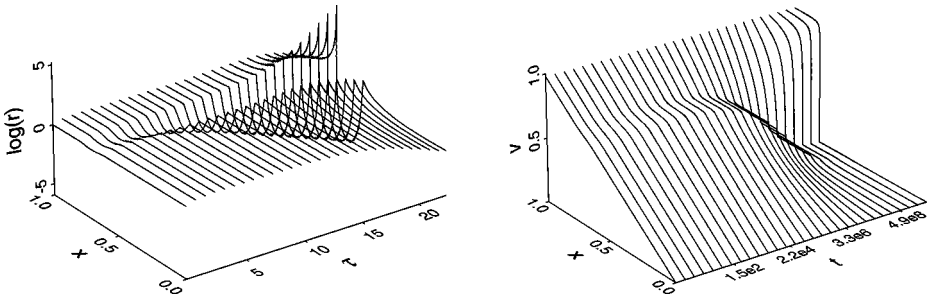**FIG. 44.** Plots of the evolution of r and v versus τ and t for Data 13.

FIG. 45. Plots of the evolution of r and v versus τ and t for Data 14.
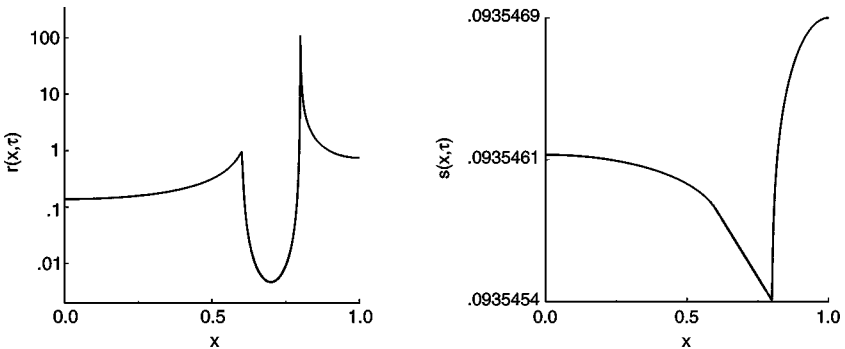

FIG. 46. Plots of $r(x, \tau)$ and $s(x, \tau)$ versus x at $\tau \approx 22$.

<div align="center">

TABLE X

The Parameter Values for Initial Data with Two Bumps

</div>

Data number	$\mathcal{W}_1$	$\mathcal{A}_1$	$\bar{x}_1$	$\mathcal{W}_1$	$\mathcal{A}_1$	$\bar{x}_1$
15	0.2	0.2	0.4	0.2	0.2	0.7
16	0.4	0.2	0.3	0.2	0.2	0.7
17	0.2	0.4	0.3	0.2	0.2	0.7

there is a kind of competition between spikes and in situations in which the solutions lack symmetry, one spike tends to dominate other spikes after a lengthy transient period.

We alter the bump data to give an initial function with two bumps, one at $\bar{x}_1$ and one at $\bar{x}_2$.

$$r_0(x)^2 = \begin{cases} 1 + \frac{16\mathcal{A}_1}{\mathcal{W}_1^4}(x - \bar{x}_1 - \mathcal{W}_1/2)^2(x - \bar{x}_1 + \mathcal{W}_1/2)^2, & \bar{x}_1 - \mathcal{W}_1/2 < x < \bar{x}_1 + \mathcal{W}_1/2 \\ 1 + \frac{16\mathcal{A}_2}{\mathcal{W}_2^4}(x - \bar{x}_2 - \mathcal{W}_2/2)^2(x - \bar{x}_2 + \mathcal{W}_2/2)^2, & \bar{x}_2 - \mathcal{W}_2/2 < x < \bar{x}_2 + \mathcal{W}_2/2 \\ 1, & \text{otherwise} \end{cases}$$

$$s_0(x) = 1.$$

(44)

We compute solutions corresponding to parameter values listed in Table X. Data 15 has the left-hand bump closer to the middle of [0, 1], Data 16 has a fatter bump, and Data 17 has a taller bump.

In each case, the corresponding solutions form two peaks initially and then one peak begins to dominate after a long transient period. We plot the evolution of the solutions for Data 15 in Fig. 47. We plot the evolution of the solutions for Data 16 in Fig. 48. Finally, we plot the evolution of the solutions for Data 17 in Fig. 49. The data suggest that taller peaks and peaks closer to the middle of [0, 1] dominate.

The degree of domination by one peak is not the same in the three solutions. This affects the convergence of the solutions to the model. We compare the parameter values in the model computed by least squares for the solutions corresponding to Data 0, 15, 16, and 17 in Table XI. In the solutions with multiple peaks, the model is fitted to the largest peak in the solution. The closeness of the fit to the model appears to be correlated to the degree that the larger peak dominates the other peak, with very good agreement for the solution corresponding to Data 17.
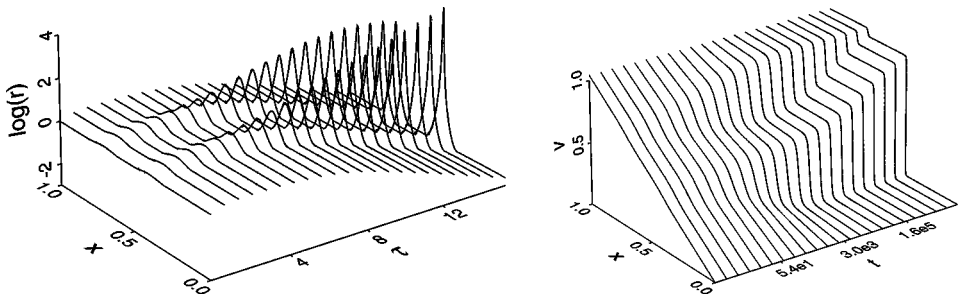

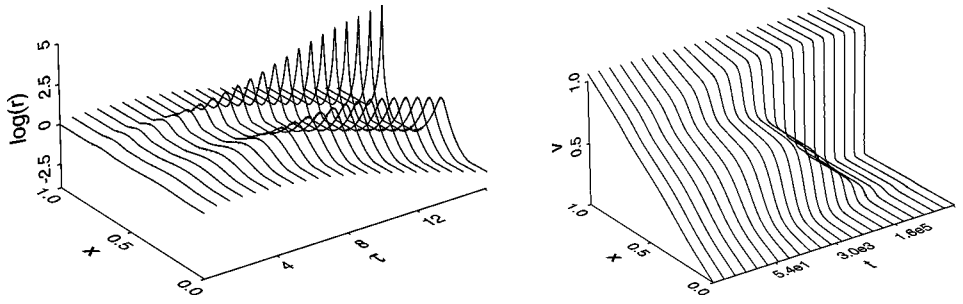**FIG. 47.** Plots of the evolution of r and v versus τ and t for Data 15.

FIG. 48. Plots of the evolution of r and v versus τ and t for Data 15.

6.4. *Varying α*

We use the value $\alpha = 2$ largely for computational reasons. Solutions for $\alpha > 2$ for the peaks that grow in height and become very narrow extremely rapidly and require excessively fine discretizations for accurate computations. On the other hand, when α approaches 1, the transient period becomes longer and longer, leading to problems with accuracy due to the accumulation of error.

The main observation about varying α is that the behavior reported on in this paper appears to depend smoothly on the value of α. For example, when α is close to 1, layers form after a very long period when there is hardly any motion in the solution. We have seen that when $\alpha = 1$, there is no smoothing nor peak formation in solutions. The slow evolution for α close to 1 is evident in the plots of the evolution of the solutions for $\alpha = 1.1$ beginning with the special data (26) shown in Fig. 50.

When α is close to 2, the corresponding solutions appear very similar to the solutions for $\alpha = 2$ while there is a close correlation in the parameters for the model determined by least squares. In Table XII, we list the parameter values for solutions for $\alpha = 1.9$, 2.0, and 2.1 starting with special data (26).

6.5. *Adding Diffusion to the Equation for r*

It is natural to wonder about the extent to which the behavior of the solutions exhibited so far depends on the singular nature of the equation for the rescaled temperature r. In
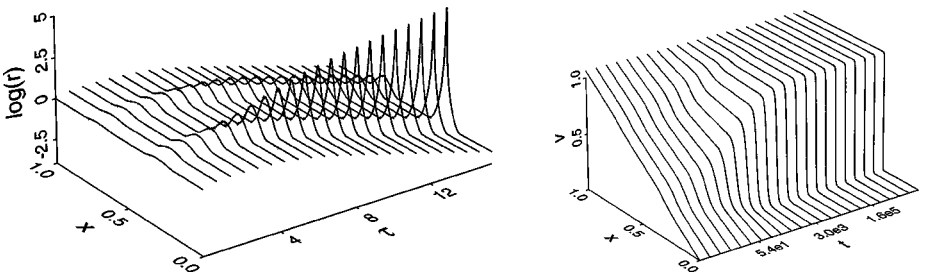

FIG. 49. Plots of the evolution of r and v versus τ and t for Data 15.

TABLE XI

The Parameter Values in the Model Functions $\tilde{r}$ and $\tilde{s}$ Computed from the Numerical Solutions Using Least Squares Line Fits

Data	σ_1	C_1	σ_2	σ_3	C_3	Predicted C_3
0	0.167	0.785	0.500	0.0831	0.792	0.798
15	0.23	1.1	0.57	0.14	0.97	0.67
16	0.19	2.4	0.53	0.096	0.46	0.18
17	0.17	2.4	0.50	0.084	0.33	0.34

Note. The correlations of the various fits were greater than 0.999999.

particular, the set of equations

$$s_\tau - r^{-\alpha}e^{\tau/(1+\alpha)}s_{xx} = \frac{\alpha}{1+\alpha}s\left(1 - (\alpha+1)r^{\alpha-1}s^2\right), \qquad 0 < x < 1, 0 < t,$$
$$r_\tau - \epsilon r_{xx} = -\frac{1}{1+\alpha}r\left(1 - (\alpha+1)r^{\alpha-1}s^2\right), \quad 0 < x < 1, 0 < t \tag{45}$$

with homogeneous Neumann boundary conditions for r and s is a natural variation of the original model (14). Here we consider ϵ to be a small diffusion parameter.

The presence of diffusion appears to regularize the solutions in the sense that a peak in r develops to a point and then becomes fixed. The maximum peak height appears to increase as ϵ decreases. We plot the maximum of $r(x, \tau)$ for three solutions starting with the special data (26) and $\epsilon = 0.001, 0.0001$, and 0.00001 along with the special solution computed above in Fig. 51. The damping effect of the diffusion on the growth of the peak is similar to that experienced by the numerical diffusion induced by coarse discretization, as in Fig. 12.

We also plot the minimum height of $r(x, \tau)$ in Fig. 51. We see that there is apparently no lasting effect on the smallest value of r from the diffusion term. This is also true of the decay rate of the value of s. In Fig. 52, we plot the maximum of $s(x, \tau)$ for the four computations.

In terms of the physical variables, a solution of (45) forms a layer that steepens to a certain point and then remains fixed after that. We plot the evolution of the solution for $\epsilon = 0.00001$ in Fig. 53.
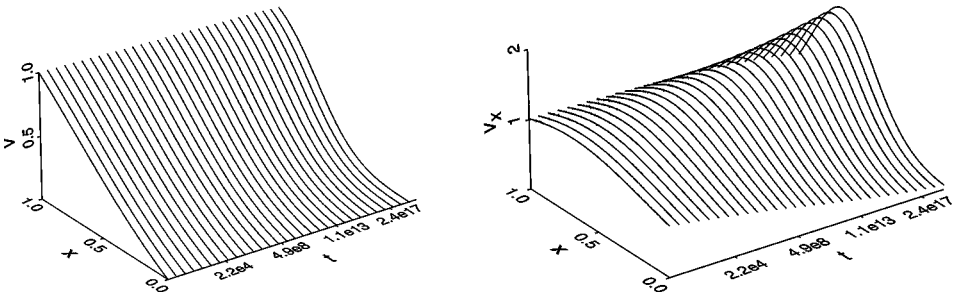

FIG. 50. Plots of the evolution of v and v_x versus τ and t for the solution with $\alpha = 1.1$ beginning with the special data (26).

TABLE XII

The Parameter Values in the Model Functions $\tilde{r}$ and $\tilde{s}$ Computed from the Numerical Solutions Using Least Squares Line Fits

α	σ_1	C_1	σ_2	σ_3	C_3	Predicted C_3
2	0.167	0.785	0.500	0.0831	0.792	0.798
1.9	0.16	0.79	0.50	0.070	0.78	0.79
2.1	0.18	0.81	0.50	0.097	0.79	0.79

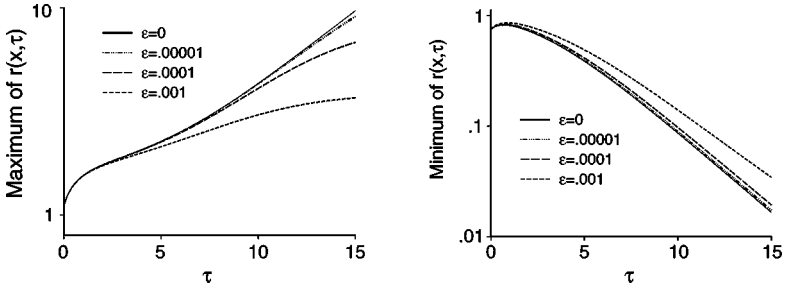*Note.* The correlations of the various fits were greater than 0.999999.

FIG. 51. Plots of the maximum and minimum of $r(x, \tau)$ versus τ for solutions of (45) starting with the special data (26) and the special solution.
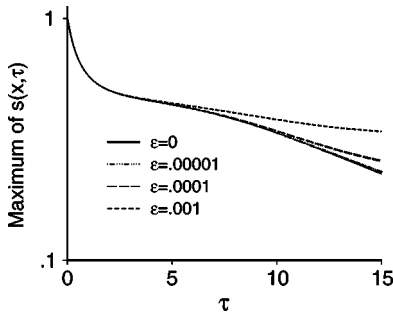

FIG. 52. Plot of the maximum of $s(x, \tau)$ versus τ for solutions of (45) starting with the special data (26) and the special solution.
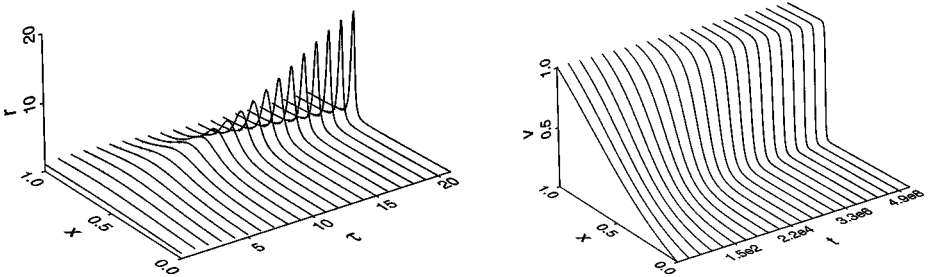

FIG. 53. Plots of the evolution of r and v versus τ and t for the solution of (45) with $\epsilon = 0.00001$.

7. CONCLUSION

The goal of this paper is to explore the role of dissipation in the large-time behavior of systems of nonlinear hyperbolic conservation laws. In particular, we are interested in the question of whether the combined dissipative effect of viscosity and thermal diffusion can counterbalance the destabilizing influence of nonlinearity. In this paper, we have investigated a fundamental system of conservation laws for a one-dimensional flow with a temperature-dependent viscosity to determine whether or not solutions that begin near a uniform shear profile develop arbitrarily sharp shear layers as time passes. We have shown that the formation of shear layers is due to the fact that viscosity decreases sufficiently quickly as temperature increases.

To analyze the fine structure of the bands we proposed a special function which solves the problem to within an extremely small residual that converges to zero exponentially quickly as time increases. The form of this function causes a shear layer to develop and this layer becomes arbitrarily sharp with increasing time. We use numerics to show that this model function is very close to being a true solution and we use the model to explain some aspects of the behavior of the solutions. We also use careful numerics to show that a wide class of solutions beginning as smooth perturbations of the uniform shear flow converge to the model function as time passes and obtain quantitative information on the rate of convergence. Finally, we consider more exotic initial data and also perturbations of the original model equations and give evidence that the phenomena we uncover are in some sense robust and generic.

REFERENCES

1. Y. Bai and B. Dodd, *Adiabatic Shear Localization: Occurrence, Theories and Applications* (Pergamon Press, Oxford, 1992).

2. R. C. Batra, Effect of material parameters on the initiation and growth of adiabatic shear bands, *Int. J. Solids Struct*. **23**, 1435 (1987).

3. R. C. Batra, Analysis of shear bands in simple shearing deformations of nonpolar and dipolar viscoplastic materials, *Appl. Mech. Rev*. **45**, 123 (1992).

4. R. C. Batra and K. I. Ko, An adaptive mesh refinement technique for the analysis of shear bands in plane strain compression of a thermoviscoplastic solid, *Comput. Mech*. **10**, 369 (1992).

5. A. Bayliss, T. Belytshko, M. Kulkarnia, and D. A. Lott-Crumbler, On the dynamics and the role of imperfections localization in thermo-viscoelastic materials, *Mod. Sim. Mat. Sci*. 941 (1994).

6. M. Bertsch, L. A. Peletier, and S. M. Verduyn Lunel, Stabilizing effects for an adiabatic rectilinear shearing of an incompressible viscous fluid, *SIAM J. Math. Anal*. **22**, 328 (1991).

7. K. Chueh, C. Conley, and J. Smoller, Positive invariant regions for systems of nonlinear diffusion equations, *Indiana Univ. Math. J*. **26**, 373 (1977).

8. R. J. Clifton, J. Duffy, K. A. Hartley, and T. G. Shawki, On critical conditions for shear band formation at high strain rates, *Scripta Met*. **18**, 443 (1984).

9. C. M. Dafermos and L. Hsiao, Global smooth thermomechanical processes in one-dimensional nonlinear thermovisoelasticity, *Nonlinear Anal. T.M.A*. **6**, 435 (1982).

10. C. M. Dafermos and L. Hsiao, Adiabatic shearing of incompressible fluids with temperature dependent viscosity, *Q. Appl. Math.* **XLI**, 45 (1983).

11. C. M. Dafermos and L. Hsiao Development of singularities in solutions of the euqations of nonlinear thermoelasticity, *Q. Appl. Math.* **XLIV**, 463 (1986).

12. J. A. DiLellio and W. E. Olmstead, Shear band formation due to a thermal flux inhomogeneity, *SIAM J. Appl. Math.* **57**, 959 (1997).

13. J. A. DiLellio and W. E. Olmstead, Temporal evolution of shear band thickness, *J. Mech. Phys. Solids* **45**, 345 (1997).

14. D. A. Drew and J. E. Flaherty, Adaptive finite element methods and the numerical solution of shear band problems, in *Phase Transformations and Material Instabilities in Solids (Madison, WI. 1983)*, Publ. Math. Res. Center Univ.-Wisconsin (Academic Press, Orlando, FL, 1984), Vol. 52, p. 37.

15. D. Edwards and D. French, Asymptotic and computational analysis of larger shear deformations of a thermoplastic material, *SIAM J. Appl. Math.* **59**, 700 (1998).

16. D. J. Estep, M. G. Larson, and R. D. Williams, Estimating the error of numerical solutions of systems of reaction–diffusion equations, *Mem. Amer. Math. Soc.* **146**, 1 (2000).

17. D. J. Estep, S. M. Verduyn Lunel, and R. D. Williams, *An adaptive finite element method for the approximation of a shear flow with temperature-dependent viscosity*, in preparation.

18. D. A. French, Computation of large shear deformations of a thermoplastic material, *Numer. Meth. Part. Differential Equations* **12**, 393 (1996).

19. D. A. French and S. M. F. Garcia, Finite element approximation of an evolution problem modeling shear band formation, *Comput. Meth. Appl. Mech. Eng.* **118**, 153 (1994).

20. J. H. Maddocks and R. Malek-Madani, Steady-state shear-bands in thermo-plasticity I. Vanishing yield stress, *Int. J. Solids Struct.* **29**, 2039 (1992).

21. A. Needleman, Dynamic shear band development in plane strain, *J. Appl. Mech.* **56**, 1 (1989).

22. J. A. Smoller, *Shock Waves and Reaction–Diffusion Equations*, 2nd ed. (Springer-Verlag, New York, 1983).

23. A. E. Tzavaras, Shearing of materials exhibiting thermal softening or temperature dependent viscosity, *Quart. Appl. Math.* **44**, 1 (1986).

24. A. E. Tzavaras, Effect of thermal softening in shearing of strain-rate dependent materials, *Arch. Rat. Mech. Anal.* **99**, 349 (1987).

25. A. E. Tzavaras, Strain softening in viscoelasticity of the rate type, *J. Integral Equations Appl.* **3**, 195 (1991).

26. J. W. Walter, Numerical experiments on adiabatic shear band formation in one dimension, *Int. J. Plasticity* **8**, 657 (1992).

27. T. W. Wright, Steady shearing in a viscoplastic solid, *J. Mech. Phys. Solids* **35**, 269 (1987).

28. T. W. Wright, Approximate analysis for the formation of adiabatic shear bands, *J. Mech. Phys. Solids* **38**, 515 (1990).

29. T. W. Wright and J. W. Walter, On stress collapse in adiabatic shear bands, *J. Mech. Phys. Solids* **35**, 701 (1987).

30. T. W. Wright and J. W. Walter, The asymptotic structure of an adiabatic shear bnad in antiplane motion, *J. Mech. Phys. Solids* **44**, 77 (1996).